1-2019

Glauconite Formation in Late Eocene ODP Site 696 Sediment in West Antarctica

Abbey States
Montclair State University

Abstract

Antarctic sediment cores collected during Leg 113 of the Ocean Drilling Program (ODP) provide important paleoclimatic evidence over the Eocene-Oligocene transition (EOT) – a period of global cooling from greenhouse to icehouse approximately 34 million years ago. The cores, collected thirty years ago, offer new research opportunities with the application of an updated age model for the EOT in West Antarctica (Houben et al., 2013). The core from ODP Site 696 in the Weddell Sea contains a complete EOT record, with a remarkably green stratum attributed to glauconite dated to the late Eocene. The sediment composition, clay mineralogy, and geochemistry of this interval was investigated in the context of recent particle size data and an improved age model.

Smear slide and X-ray diffraction analyses confirm the green mineral is an authigenic, incipient form of glauconite with a minor contribution of expandable montmorillonite to the clay fraction. Major and trace element analysis show deposition occurred under reducing, suboxic conditions with low detrital input for samples with a high fraction of glauconite. Alteration of illite by Fe^{2+} substitution is the likely formation mechanism, possibly catalyzed by an increase in oceanic productivity. The highest-glauconite sediment interval, dated to ~34.5-35 mya, suggests a marine transgression peak in the South Orkney Microcontinent region during this time caused by crustal subsidence prior to the onset of full continental glaciation. These results document early effects of ice sheet advance in the Weddell Sea, though more research is needed to determine whether the impacts are caused by glaciation from East or West Antarctica.

MONTCLAIR STATE UNIVERSITY

Glauconite Formation in Late Eocene ODP Site 696 Sediment in West Antarctica

by

Abbey States

A Master's Thesis Submitted to the Faculty of

Montclair State University

In Partial Fulfillment of the Requirements

For the Degree of Master of Science

January 2019

Thesis Committee:

College of Science and Mathematics

Earth and Environmental Studies

Dr. Sandra Passchier
Thesis Sponsor

Dr. Matthew Gorring
Committee Member

Dr. Huan Feng
Committee Member

GLAUCONITE FORMATION IN LATE EOCENE ODP SITE 696 SEDIMENT IN WEST ANTARCTICA

A THESIS

Submitted in partial fulfillment of the requirements
For the degree of Master of Science

by

Abbey States

Montclair State University

Montclair, NJ

2019

Table of Contents

List of Figures

APPENDIX

List of Tables

APPENDIX

Introduction

Antarctic sediment provides extremely robust paleoclimatic records due to the significant glacial advance and retreat that occurs with historical climate changes. These glacial cycles cause detrital sediment input and seawater geochemistry to fluctuate in response to increasing ice sheet mass, ice-rafted debris, or meltwater. Sediment diagenesis preserves the unique mineralogical characteristics and benthic foraminifer assemblages as strata are buried over time, which then documents the ancient climate record in oceanic drill cores. Climate models created from drill core studies are refined as additional data is collected from high-latitude sites near present-day ice sheets, which contributes to the understanding of critical time periods. The importance of producing accurate climate models cannot be understated since they connect the global carbon cycle with the climate record and can help predict the consequences of future increasing carbon dioxide concentrations (Zachos et al., 2008).

Significant evidence has been documented from Antarctic drill sites in support of a transition from a greenhouse to icehouse environment that occurred approximately 34 million years ago (mya) during the Eocene-Oligocene Transition (EOT) (Ehrmann and Mackensen, 1992; Zachos et al., 2001; Houben et al., 2013). High-resolution isotopic studies point to a step-wise onset of glaciation on Antarctica (Coxall et al., 2005), however the mechanism and timing of ice sheet advancement, particularly in West Antarctica, remains unclear.

Many recent studies have been conducted on core 696, collected from West Antarctica during Leg 113 of the Ocean Drilling Program (ODP), since the Southern Ocean's biostratigraphic model was updated by Houben et al.'s (2013) analysis of plankton, including particle size analysis (Light, 2017 and Lepp, 2018), geochemistry (Lepp, 2018), and thermo-geochronology (Carter et al., 2017) of samples coinciding with the EOT interval. The clay mineralogy in the core's EOT samples, however, has not been revisited following a low-resolution characterization of the whole core when samples were first collected (Robert and

Maillot, 1990). The clay mineral assemblage in this interval is of particular interest due to an extremely green layer of sediment attributed to glauconite, a mineral which can have significant palaeoclimatic implications; on-board estimates were 2-3x higher than in other intervals where glauconite was observed during Leg 113 (Barker et al., 1988). The aim of this study is to confirm that the green-colored sediment does in fact contain glauconite, determine the mechanism of its formation in and/or transport to the core location, and use the results to further refine our understanding of the EOT onset in West Antarctica.

Eocene Oligocene Transition

The transition from a global greenhouse to ice house began in the late Eocene with the first major extinction of warm water taxa (Prothero, 1994). During this period in the middle-late Eocene, rifting between Antarctica and Australia occurred and the formation of glaciers on Antarctica was initiated; the "Terminal Eocene Event" at ~34 mya brought only minor extinctions in planktonic foraminifera (Prothero, 1994). Early Oligocene deterioration ~33 mya is associated with most foraminifera extinctions and evidence of massive cooling and deep marine erosion as circulation was enhanced around the Antarctic continent, stimulating deep water production (Prothero, 1994). The largest sea level drop in the entire Cenozoic occurred during the mid-Oligocene marine regression with major Antarctic glaciation, massive deep-sea erosion, and further oceanic cooling (Prothero, 1994). During the Oligocene, widespread glaciation occurred, but a stable Antarctic ice cap wasn't established until the middle Miocene (~11-14 mya) (Kennett, 1977).

Evidence for the EOT has been well-documented from East Antarctic sediment cores (Galeotti et al., 2016; Passchier et al., 2017). Stable carbon isotopes have been used to reconstruct atmospheric CO_2 at the time of sediment deposition, showing a significant decrease in pCO_2 over the EOT (Pagani et al., 2005; Zachos et al., 2001). $\delta^{13}C$ studies also show that the development of major Antarctic continental ice sheets in the early Oligocene was accompanied by a dramatic

increase in the carbonate compensation depth (CCD) (Coxall et al., 2005). Cooling ocean temperatures are reflected in changes in nannofossil and dinocyst assemblages and an increase in oceanic productivity (Houben et al, 2013; Villa et al., 2013). The presence of ice-rafted grains and shifts in clay mineralogy provide evidence for the onset of Antarctic glaciation during the early Oligocene (Ehrmann and Mackensen, 1992).

Benthic foraminifera oxygen isotopes have been used for high-resolution palaeoclimate reconstructions, since higher $\delta^{18}O$ values correlate with colder temperatures as the lighter isotope of oxygen ($\delta^{16}O$) is preferentially sequestered in glacial ice (Lea, 2006). Higher relative benthic foraminifera $\delta^{18}O$ concentrations in deep sea sediment therefore correlate with an increase in high-latitude ice sheet volume. $\delta^{18}O$ records reflect both 1) the periodic variations in Earth's orbit that influence seasonal ice sheet growth and 2) anomalous climate events associated with extreme isotopic variations (Zachos et al., 2001). These isotopic studies indicate that the onset of the EOT occurred in two major steps approximately 200 thousand years apart, as shown in Figures 1 and 2, and the initiation of widespread ice sheets were triggered by low-amplitude changes in Earth's obliquity cycle (Coxall et al., 2005).

A)

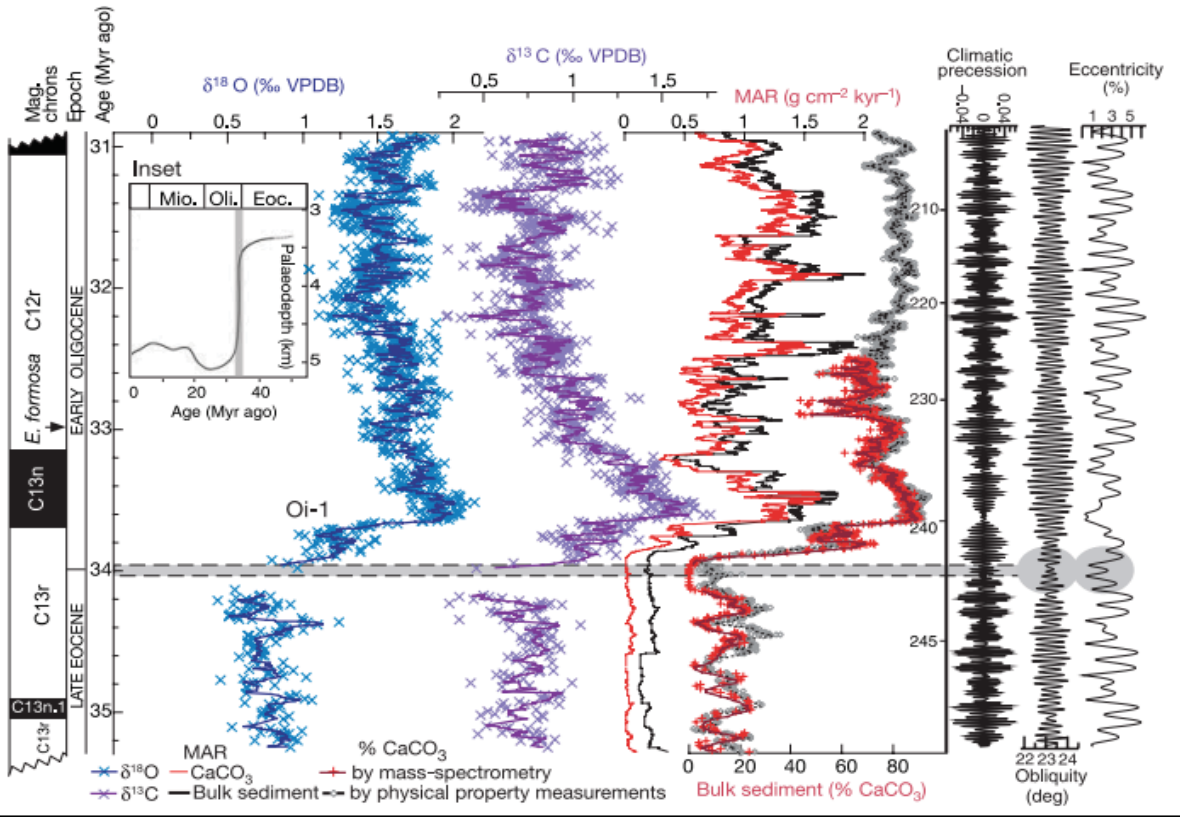

B)

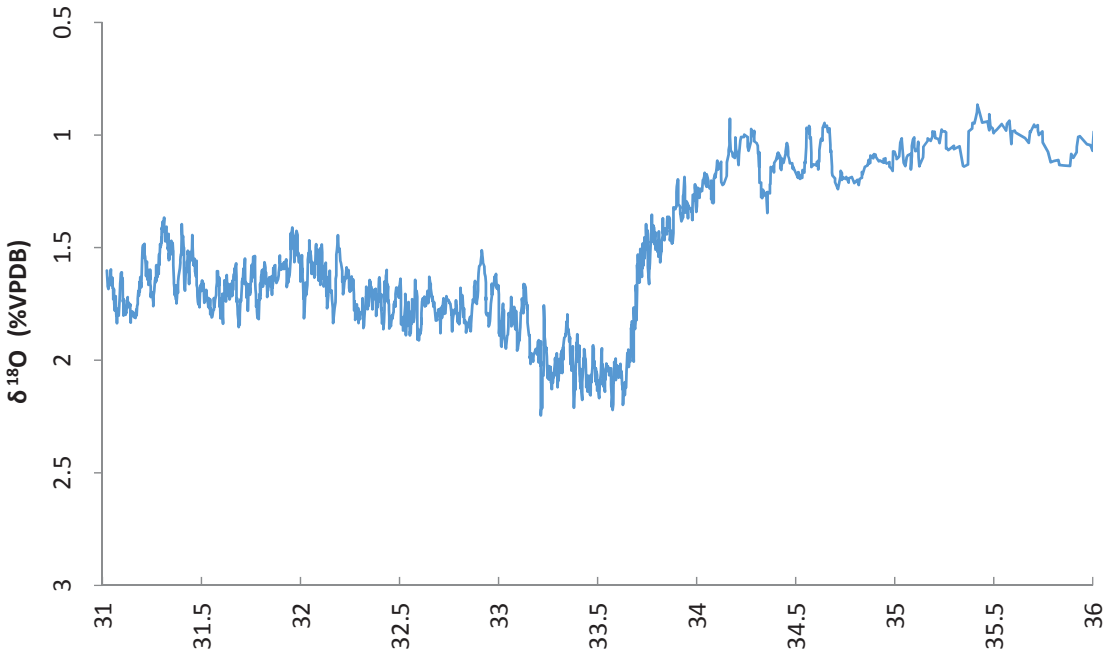

Figure 1: A) Changes in global climate and ocean chemistry as recorded by high-resolution studies of $\delta^{18}O$ and $\delta^{13}C$ at Deep Sea Drilling Project locations. The inset shows a 1 km deepening of the calcite compensation depth (CCD) at the onset of the EOT (Coxall et al., 2005). B) Detail of $\delta^{18}O$ fluctuations over the EOT interval based on Coxall et al. (2005) on updated timescale GTS2012 (Veizer and Prokoph, 2015)

West Antarctica Regional Geology

Land on the present-day Antarctic continent is 98% covered by an ice sheet ranging from 1-4 km in thickness, and its history has been recorded from studies of the continental margins offshore (Anderson, 1999). East and West Antarctica are separated by the Transantarctic Mountain range, which spans 3,500 km across the continent. Formation of East Antarctica began in the Early Archean, and was stabilized into its Gondwana configuration in the Proterozoic. West Antarctica is a more complex, recent formation and consists of four to five separate crustal blocks: Marie-Byrd Land, Ellsworth-Whitmore Mountains, Antarctic Peninsula, Thurston Island, and Haag-Nunataks (included by some researchers) (Anderson, 1999). The exact positioning of these blocks prior to the breakup of Gondwana is unclear, but their present locations were established by the early Cenozoic (Lee et al., 2012). During the Cenozoic, the Antarctic continent became isolated by the widening of Drake Passage as Australia moved north in the Early Eocene (Kennett, 1977).

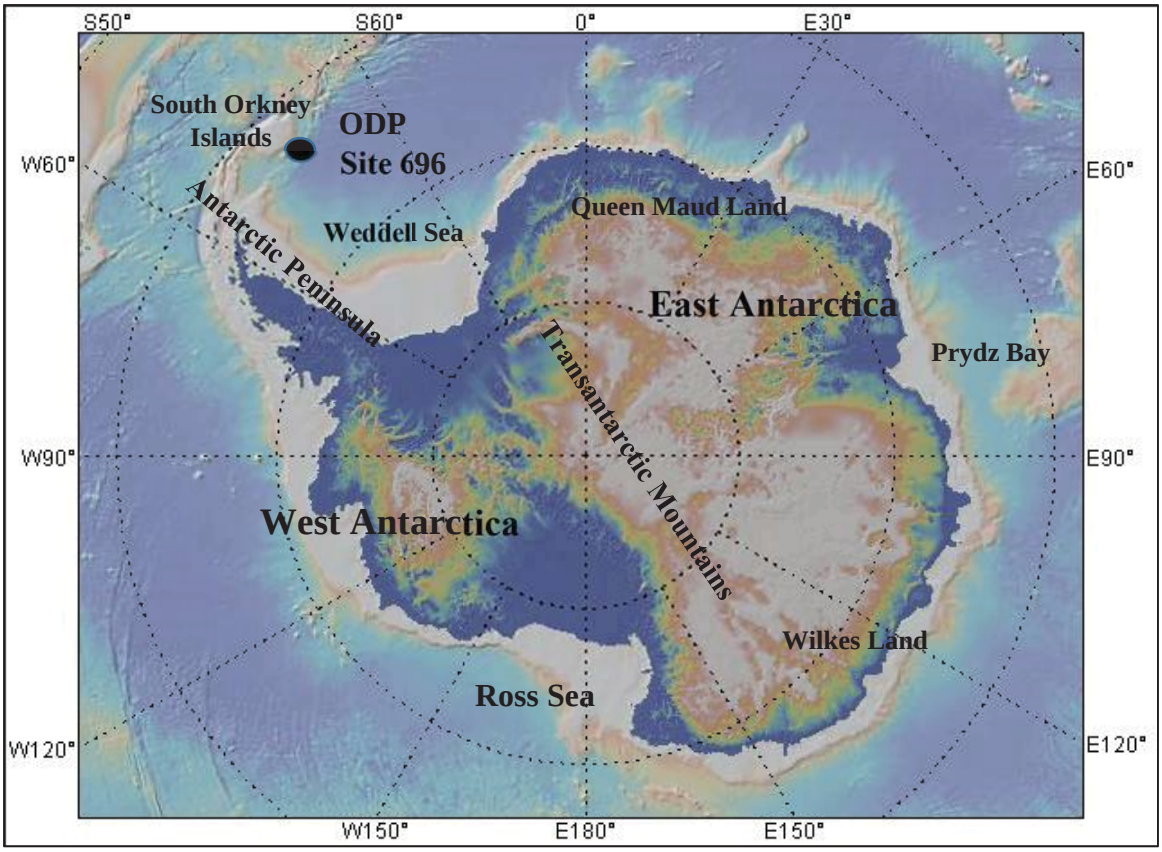

Figure 2: GeoMap App rendered map of the Antarctic continent, including topography and ice-sheet thickness as depicted by Bedmap2 layer (British Antarctic Survey, 2018), with notable locations labeled.

The study area is located on the southeastern portion of the South Orkney microcontinent (SOM) on a continental shelf margin in the Weddell Sea in West Antarctica. Islands near the SOM consist of mainly metasedimentary and meta-igneous rocks deposited on the Pacific margin of Gondwanaland before the Gondwana breakup (Trouw et al., 1997). After the Gondwana breakup and through the EOT, the Scotia arc formed a continuous connection between Antarctica and South America and prevented the establishment of the circumpolar current until the early Oligocene (Trouw et al., 1997). Currently, the SOM is located in an “Iceberg Alley,” a drift trajectory confluence of icebergs originating from both East and West Antarctic ice sheets (Anderson, 1999). This region is down-current from both the Antarctic Peninsula and West

Antarctica. During the EOT, the SOM was much closer to both West Antarctica and South America than it is today (see Figure 3).

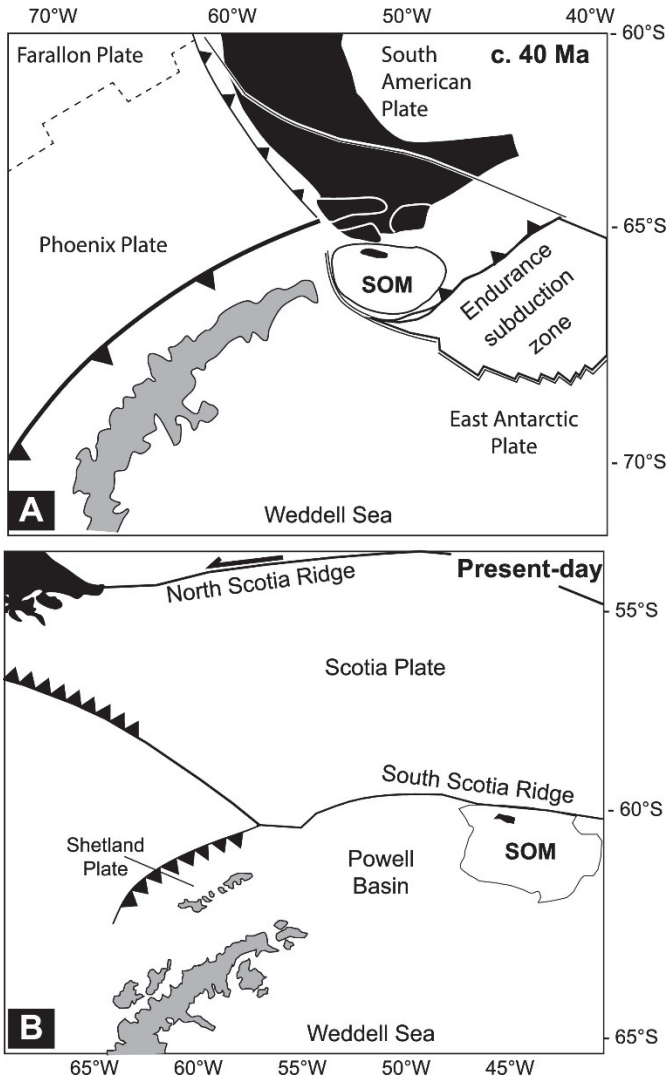

Figure 3: A) the position of the South Orkney Microcontinent (SOM) during the middle-late Eocene and B) the present day SOM location (Carter et al., 2017)

Study Site

This study is focused on Site 696, which was cored from February 23 to March 7, 1987 as part of Leg 113 of the Oceanic Drilling Program (ODP). The initial goals of this core location were to 1) collect data to inform the history of the calcite compensation depth close to the West

Antarctica margin, 2) assess ice-rafted debris and clay composition to provide information about the climatic history and paleoglacial development in this region, 3) study the development of the Antarctic Convergence through the biosiliceous record of the Neogene, and 4) examine whether the late Oligocene/Neogene opening of Drake Passage impacted sediment deposition at Site 696 (Barker et al., 1988).

Core 696A was drilled to 103 meters below sea floor (mbsf), and core 696B was drilled from 76.6 to 645.6 mbsf with a 27.5% total recovery (Barker et al., 1988). Ice-rafted debris was recorded as common down to 366 mbsf, and rare below this depth with the exception of two stratifications between 530 and 570 mbsf. Calcareous nannofossils were observed in sediment dated to the Paleogene, but siliceous microfossils were not present.

Core 696B was subdivided into seven units; unit VII is the base of the core, from 529.8 to 645.6 mbsf and consists of four subunits. Subunit VIIA is sandy mudstone and tentatively dated to the Miocene, subunit VIIB and VIIC are claystone, clayey mudstone, and silty mudstone tentatively dated to the upper Oligocene to lower Miocene, and subunit VIID is sandy mudstone dated to the upper Eocene to lower Oligocene (Barker et al., 1988). A high abundance of green sediment attributed to glauconite was also observed in subunit VIIC samples.

The dating of this core interval was based on biostratigraphy observed in smear slides, but the uncertainty was significant due to paucity of fossils present as well as disturbance and poor sediment recovery (Bryant and Rack, 1990). Houben et al. (2013) later revised the estimated depth of the EOT in this core based on an observed plankton ecosystem reorganization in marine fossil dinoflagellate cysts (updated dating and lithology on Figure 4).

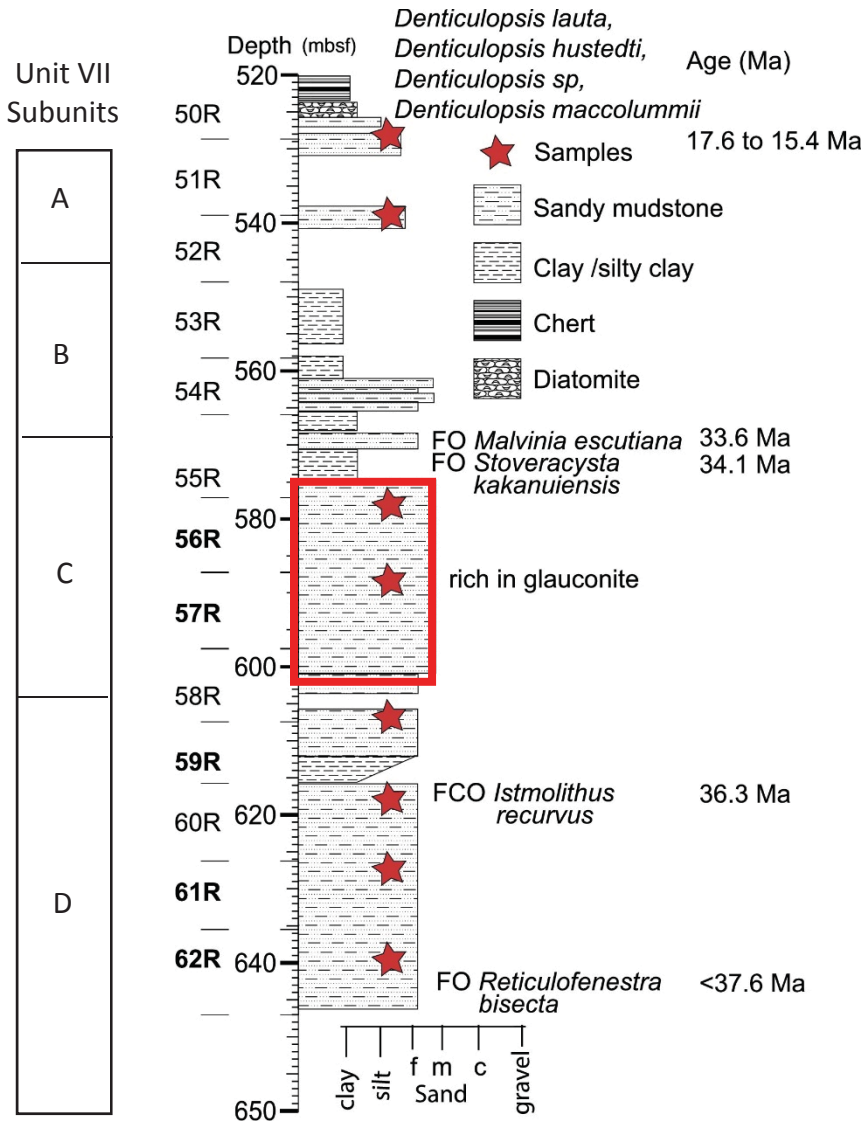

Figure 4: Lithology and dating for core 696 adapted from Carter et al. (2017). The red box highlights the interval examined in this study. Stars indicate sample depths studied by Carter et al. (2017).

Of the ODP Leg 113 sites (see Figure 5 below), the glauconite observed at Site 696 is uniquely high, up to 45%. Glauconite was also observed at proximal ODP Sites 695 and 697 from the same expedition, however only to a maximum of four percent (Barker et al., 1988). A 25% glauconite sample dated to the Albian was recorded at Site 693, the highest of all other Leg 113 samples. Samples collected from the EOT at other core sites during Leg 113 contained a maximum of 10% glauconite.

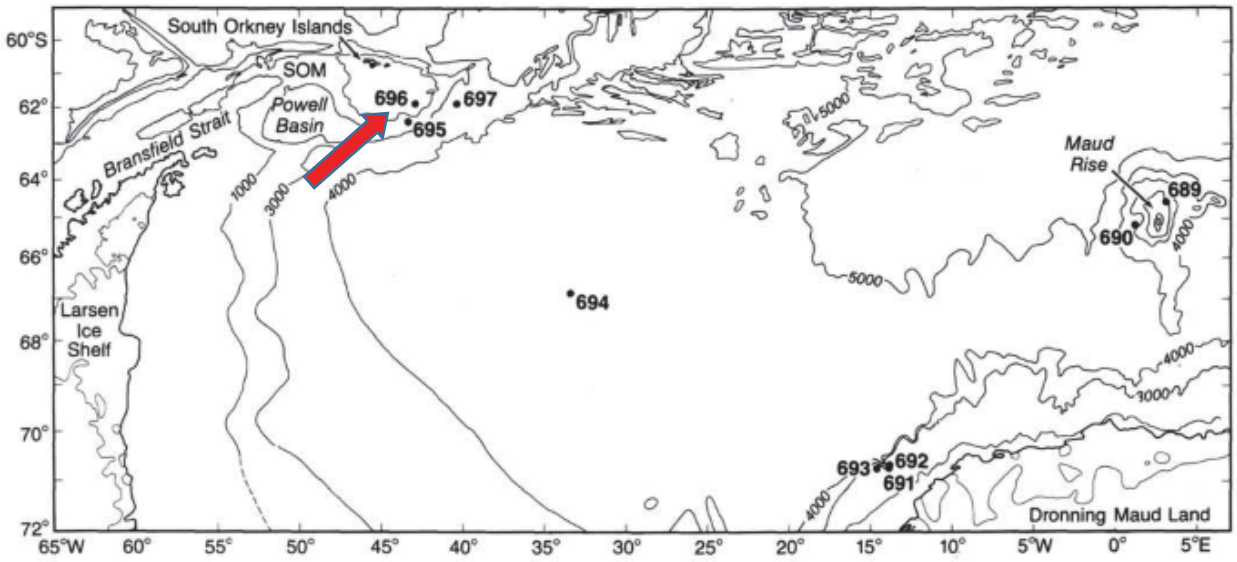

Figure 5: Regional setting of Site 696 on the northeastern margin of the Weddell Sea (after Barker et al., 1988)

Previous Work on Core 696

The core from study Site 696 has been extensively studied since it was collected in 1987. The ODP expedition prepared smear slides to record lithology of all samples, physical properties were analyzed from the most intact portions of the core, X-ray diffraction (XRD) analysis was conducted on select core samples for an overall distribution of clay minerals, and four dropstones were collected from the upper portion of the core for petrographic analysis (Barker et al., 1988).

Initial XRD analyses were performed at a rate of one sample per 10-meter core interval with the goal of identifying the major paleoenvironmental changes expressed by clay mineral assemblages (Barker et al., 1988). Further XRD and geochemical analyses for major elements were conducted by Robert and Maillot (1990) at a rate of two samples per core interval (see Figure 6). The one significantly glauconite-bearing sample analyzed (57R-1) was identified as having 100% poorly crystallized illite contributing to the clay mineral sediment fraction, with significant K, Fe, and Mg contents and other major element indicators that suggested the sediment is mainly authigenic (Robert and Maillot, 1990). A local shallow water emergence was

suggested as the source of the glauconitic stratum in both samples, where detrital smectite was transformed by a K-rich alkaline tidal environment by periodic flooding and drying, as was identified by Deconnick et al. (1988). The XRD results were also compared to the clay associations observed at other sites in the Weddell Sea and Falkland Plateau area, and similar clay mineral proportions were observed in EOT sediments (Robert and Maillot, 1990).

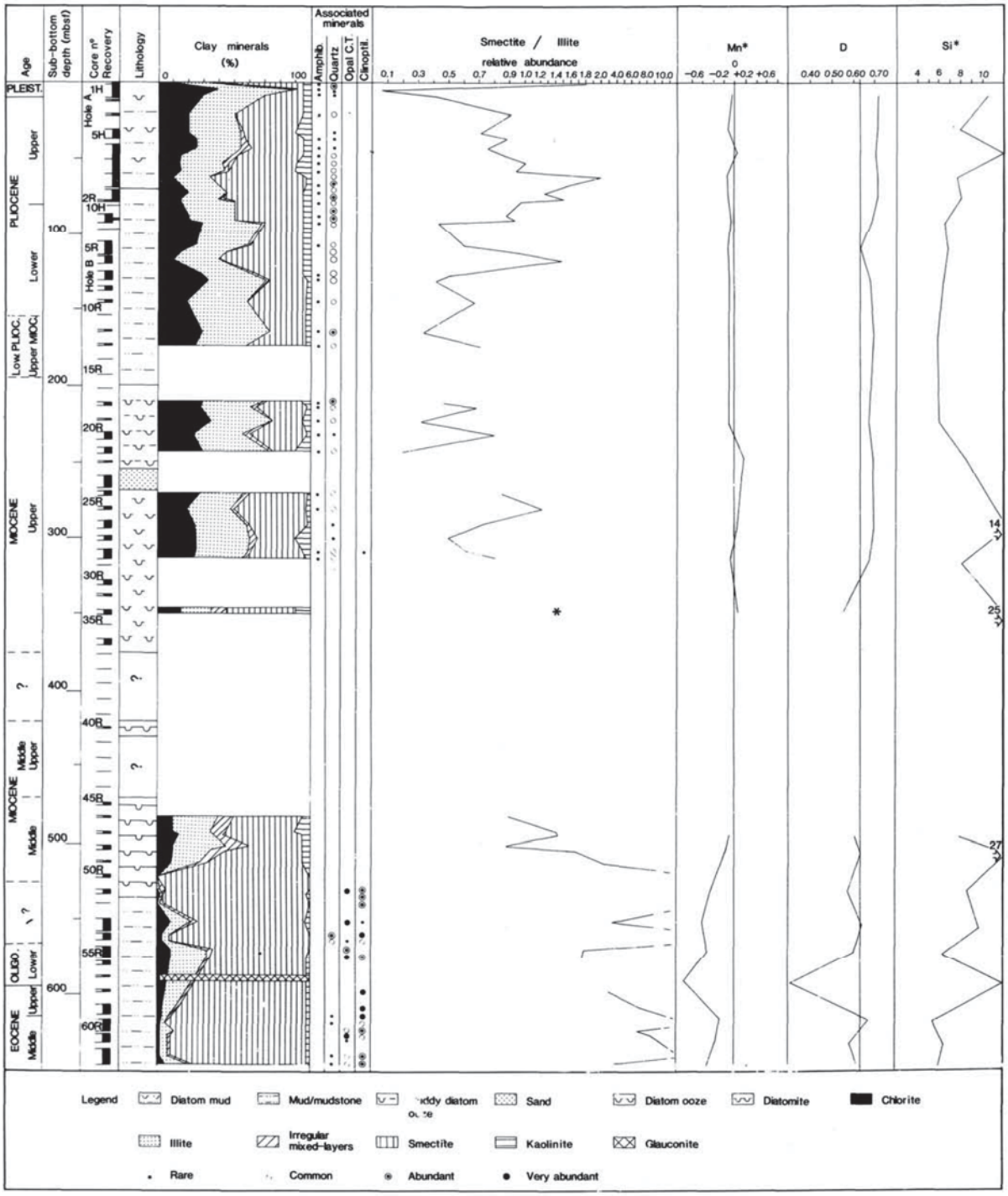

Figure 6: Clay mineral and geochemical data from the initial analysis of core 696 (Robert and Maillot, 1990)

Houben et al. (2013) used core 696 and several sites in East Antarctica to revise the age model for the onset of glaciation based on marine dinoflagellate cyst fossils, finding an abrupt restructuring of Southern Ocean plankton beginning with the earliest Oligocene (33.6 million years ago). The estimate of the EOT boundary in the core was adjusted from ~600 mbsf (Barker et al., 1988 and Robert and Maillot, 1990) to ~570 mbsf (see Figure 12) which marks a plankton assembly shift from dominant Transantarctic dinocysts to protoperidiniacean taxa and the first occurrence of *M. escutiana* (Houben et al., 2013). Figure 7 summarizes the dating of core 696 EOT samples used for this study based on results from Houben et al. (2013). Study samples were calculated to range in age from approximately 35.3 to 34.3 mya; all sample dates are presented in Table A-1 in the Appendix.

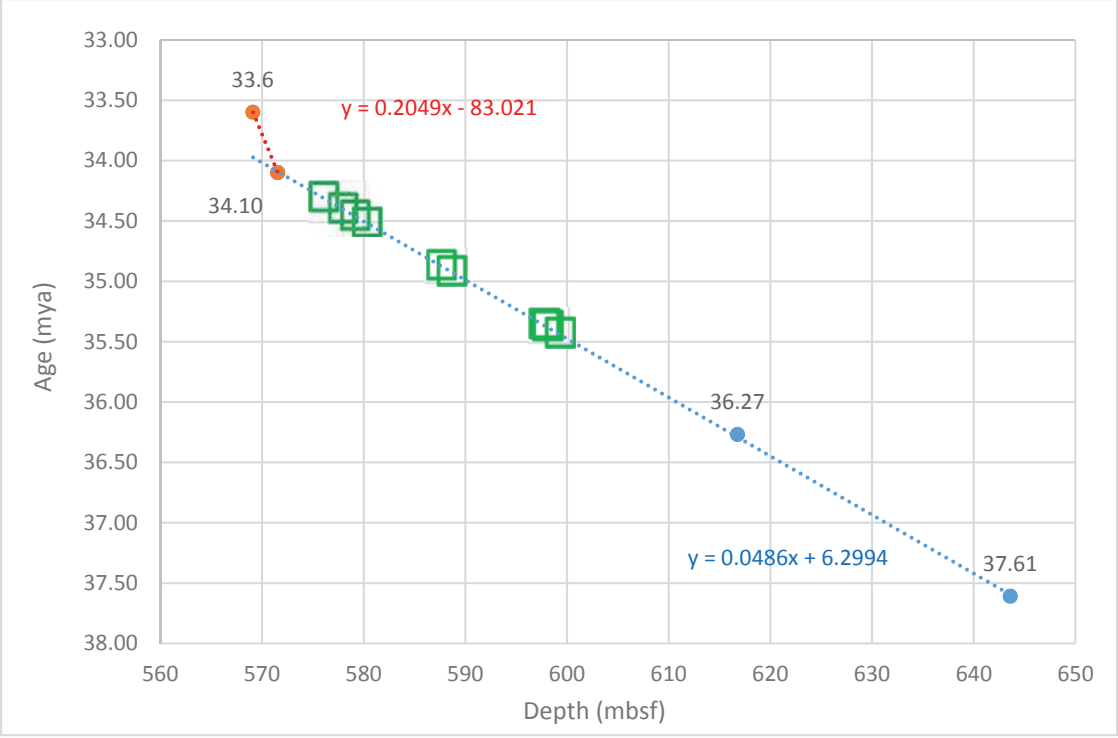

Figure 7: Age-depth plot for Site 696 based on model from Houben et al. (2013). Study samples are represented by the green boxes with dates calculated from sample depths and trendline based on Houben et al. (2013) Eocene samples (in blue).

Carter et al. (2017) studied the sand grains in Site 696 EOT samples using petrographic analysis, geochronological, and thermochronological dating to identify sand provenance. The sand fraction of the sediment was found to be transported by ice from the southern Weddell Sea region rather than of local origin, between the Ellsworth-Whitmore Mountains in West Antarctica and the Dronning Maud Land in East Antarctica, which provided evidence for glacial calving in the Weddell Sea embayment 2.5 million years before the $\delta^{18}O$ event commonly considered to mark the onset of glaciation (Carter et al., 2017).

Laser particle size analysis was conducted on the majority of samples identified for this study and documented by Light (2017) (see Figures 8-10). This study concluded that the core 696 EOT interval contained overall finer sediment when compared to East Antarctic core intervals dated to the EOT, which indicates that the 696 site was a deeper shelf at the time of deposition. Light (2017) also identified overall higher particle size variation over the core 696 EOT interval than what was reported for the East Antarctic cores. High-resolution particle size and geochemical analysis was also conducted by Lepp (2018) over the 55R core interval, just above the samples selected for this study, over the revised EOT boundary. Additional evidence was found in support of a cool, dry climate with a significant glacial contribution to sediment during the EOT deposition period that is consistent with East Antarctic EOT sediment, despite conflicting evidence for a later onset of glaciation in West Antarctica (Lepp, 2018). A summary of the particle size results for samples used in this study is presented in Table A-2 in the Appendix.

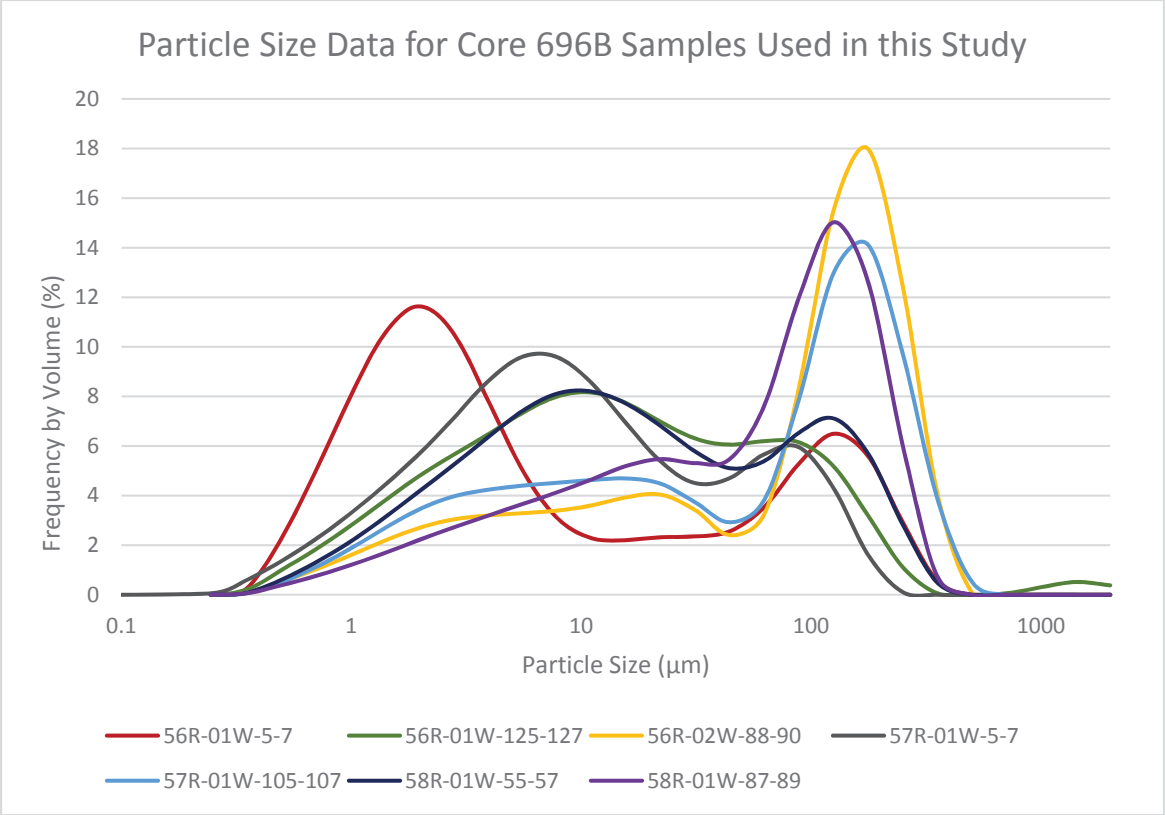

Figure 8: Frequency in volume percent of particle size (microns) (Light, 2017) for core 696B samples used in this study.

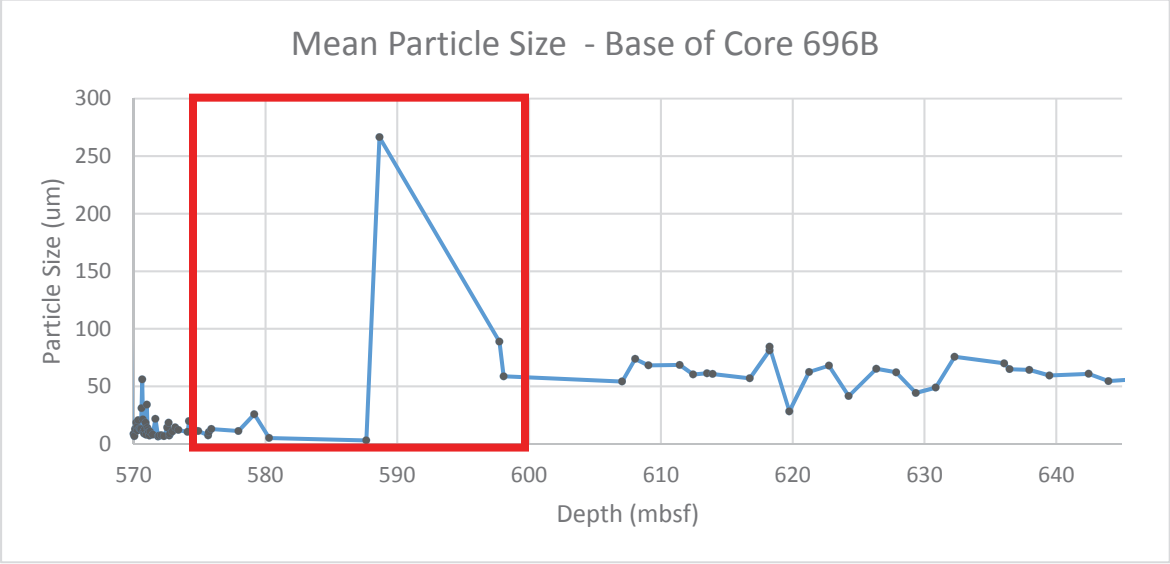

Figure 9: Mean particle size (microns) of samples at the base of core 696B (data combined from analyses by Light [2017] and Lepp [2018]). The red box indicates the interval that was analyzed in this study.

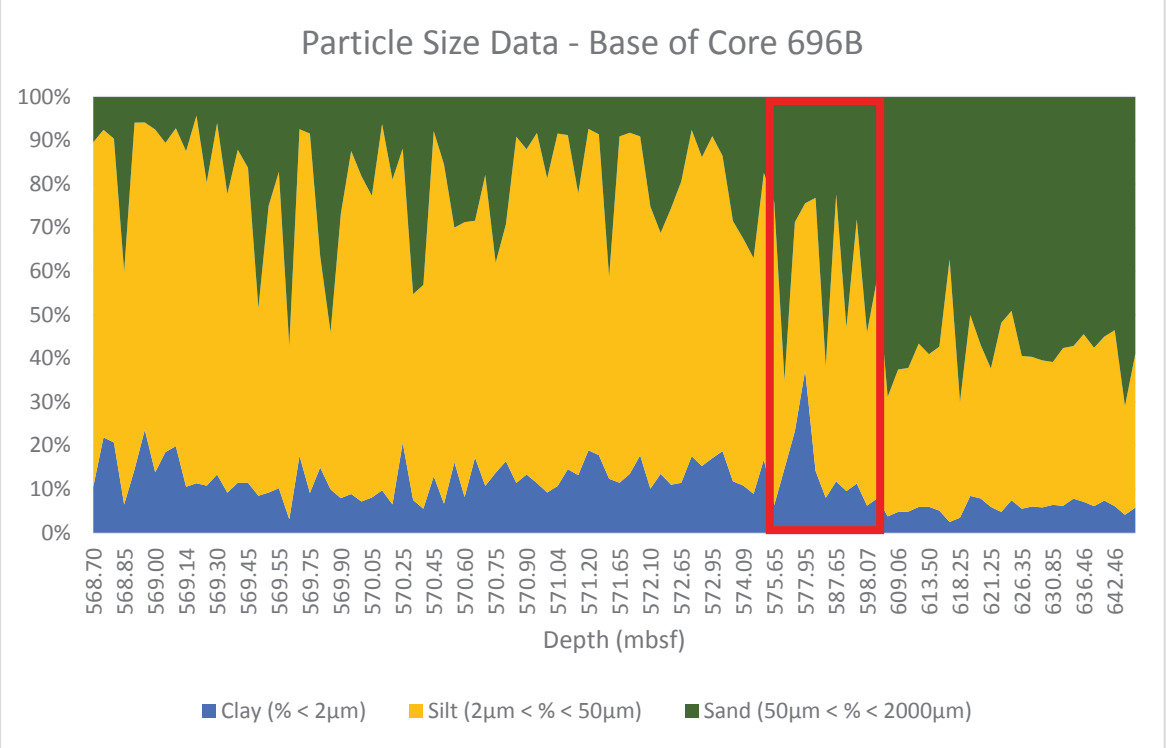

Figure 10: Frequency in volume percent of clay, silt, and sand in samples from the base of core 696B (after Light [2017] and Lepp [2018]). The red box indicates the interval that was analyzed in this study.

Green Clay Minerals

As discussed in the previous section, several studies to-date have analyzed the petrology, geochronology, and geochemistry of Site 696 EOT sediment, however none have examined the remarkably green clay-bearing stratum located at ~580-600 mbsf in detail and the potential mechanisms for its formation. Low-resolution XRD studies have analyzed the core's clay fraction (Barker et al., 1988; Robert and Maillot, 1990), and in each case, the clay in this interval was 100% attributed to glauconite with the assumption that it was formed in shallow waters affected by tidal influence. However, the identification of clay minerals using a single analytical technique is difficult and can be inconclusive due to their characteristic amorphous crystallinity, and a multi-evidence approach can aid in identification. Glauconite is the only known clay mineral occurring in sediment that is authigenic, abundant, and impurity-free (Triplehorn, 1965), and is typically considered to be an indicator of low sedimentation rates (Amorosi, 1997). Low

sedimentation rates in a high-latitude continental margin would indicate minimal glacial influence on the sediment, since glaciers are associated with significant rock flour transported by meltwater streams. Therefore, the formation of glauconite in Site 696 sediment is critical to understanding the paleoclimate conditions of the South Orkney Microcontinent during the EOT.

Definitive identification of minerals in clay is more difficult than silt or sand; a petrographic microscope's resolution is approximately 2μm, and therefore clay minerals (defined as containing crystals < 2μm) cannot be identified using optical observations alone (Velde, 2005). Green clays can be easily identified in a hand sample, however they appear as a mass of unidentifiable grains in a thin section or smear slide (Velde, 2005). Since green clays are also chemically similar and nonstoichiometric, traditional geochemical analysis cannot be used to distinguish between different minerals since it is unable to determine oxidation states.

Glauconite is a hydrated iron-rich micaceous clay mineral that is related to illite; the term glaucony is also used as a morphological term describe sand-sized greenish earthy pellets in sedimentary rock that may not consist exclusively of mineralogical glauconite (McRae, 1972). The illite group consists of non-expanding dioctahedral micaceous clay minerals with a tetragonal-octahedral-tetragonal structure (Poppe et al., 2001, see Figure 11). Glauconite is the green, iron-rich illite group member and occurs primarily in pelletal form (Poppe et al., 2000). Grains consist of random interstratification of nonexpanding 10 Å layers with generally less than 10% expandable smectite layers (McRae, 1972). Glauconite's crystal structure does not respond to typical supplemental treatments that are used for clay mineral analysis using XRD (e.g. ethylene glycolation and heat treatment at 400ºC and 550 ºC) (Poppe et al., 2001). Glauconite and illite both correspond very closely to ideal dioctahedral structures (Ireland et al., 1983). The two main differences between the minerals are: 1) illite has a better inverse relationship between Mg and Al in the octahedral layer and 2) glauconites have higher interlayer cation occupancies (Moore and Reynolds, 1997).

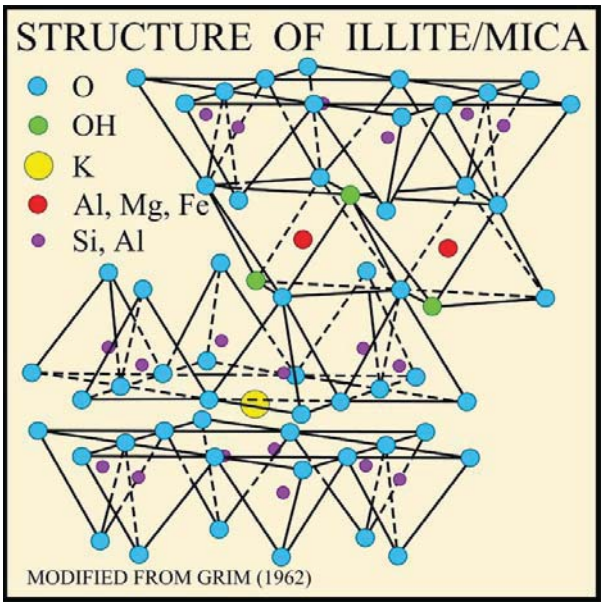

Figure 11: Crystal structure of the illite/mica group (Poppe et al., 2001)

Glauconite forms initially only by direct precipitation and not transformation (Odin, 1988), however both authigenic and allogenic deposits have been found in a wide range of modern marine environments. Authigenic glauconite generally forms in modern marine sediments between 50ºS and 65ºN, with accumulation occurring between the outer shelves and continental slopes at the sediment interface (Moore and Reynolds, 1997). In some ancient sediment, however, glauconite has been found in known high-sedimentation and high energy shallow water deposits (Hugget et al., 2017; Chafetz and Reid, 2000; Force and Cannon, 1988; Deconnick et al., 1988). Depth and temperature of seawater are therefore not necessarily constraining factors for glauconite formation (Cloud, 1955).

Glauconite can only form under stable conditions where sediment resides for long periods of time between oxidizing and reducing environments where dissolved iron is readily available (Ireland et al., 1983). The mechanism of authigenic glauconite formation has been proposed as: montmorillonite in reducing conditions -> nontronite + K(Ca, Mg) - >glauconite (Md) + pressure and aging -> glauconite (1 M) (Carroll, 1970). The final recrystallization is, for the most part,

abrupt, and no further transformation of the mixed-layer smectite component occurs, unlike the smectite/illite layers involved in the formation of chlorite (Velde, 2005).

The color of green clay minerals, such as glauconite, is generally a result of "mixed valence" formation, when some iron is reduced from Fe^{3+} to Fe^{2+} and enters into a silicate's crystal structure (Velde, 2005). Under oxidizing conditions (for example, at the surface or near-surface), iron can clump together and exit the mineral, appearing orange/brown (Velde, 2005). Since marine sedimentary environments are generally reducing conditions, burial diagenesis can further increase the reduction of iron and its presence in silicate minerals (Velde, 2005). The presence of organic material in sediment creates a reducing microenvironment which can provide optimal conditions for glauconite diagenesis (Moore and Reynolds, 1997).

Authigenic glauconite-bearing sediments generally have higher relative concentrations of potassium oxide (and a smaller distance between the corresponding XRD peaks), lower concentrations of calcium, strontium, and iron oxide, larger and more angular grains, and more concentrated spatial deposits when compared to highly-evolved forms of the mineral (Amorosi, 1997). Nascent glauconite grains forming in fecal pellets may become enriched in K and Fe in less than ten years; slightly evolved granules take 10^4 years to form, and a mature pellet takes 10^5-10^6 and up to 5 million years (Hugget, 2013).

Methodology

Sample Selection

Samples were chosen for this study based on proximity to the EOT depth estimated by Houben et al. (2013) and the amount of observed glauconite in the original ODP expedition log (Barker et al., 1988), as depicted in Figure 12. This study targets the samples where a temporary increase in glauconite is observed in the interval between Barker et al.'s (1988) original estimate of the EOT boundary and Houben et al.'s (2013) revised estimate: 55R-01W-39-41 (576.09 mbsf), 56R-01W-5-7 (577.95 mbsf), 56R-01W-125-127 (579.15), 56R-02W-88-90 (580.28 mbsf), 57R-01W-5-7 (587.65 mbsf), 57R-01W-105-107 (588.65 mbsf), 58R-01W-55-57 (597.75 mbsf), 58R-01W-87-89 (598.07 mbsf), and 58R-02W-55-58 (599.25 mbsf).

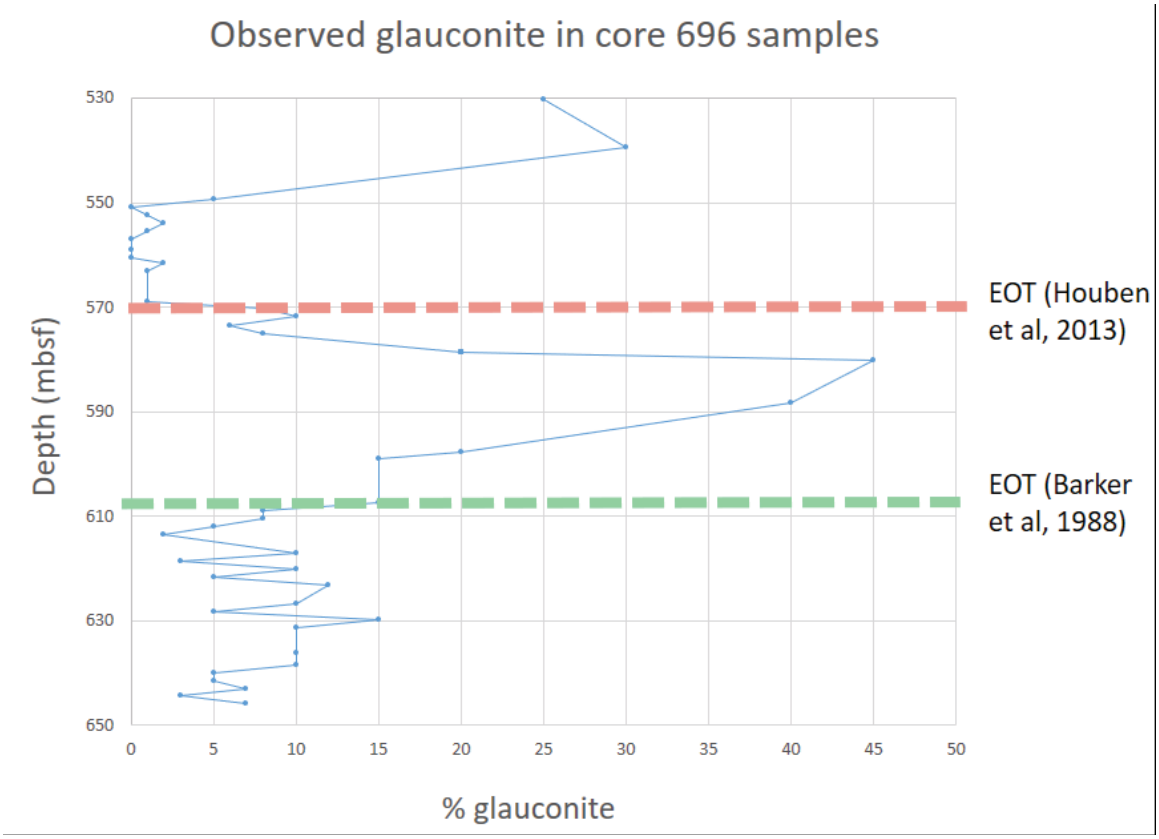

Figure 12: Observed glauconite and sample depths from smear slides analyzed by Barker et al, 1988 from the core 696 interval corresponding with the EOT; boundary estimates are included from Barker et al, 1988 and Houben et al, 2013

Smear Slides

The smear slide technique is critical to the characterization of unlithified, fine-grained sediments to identify major and minor lithologies and other isolated components that may be present (Marsaglia et al., 2013). Smear slides of core 696B samples were prepared onboard the ODP expedition in 1988, however the core log descriptions are not very detailed (Barker et al., 1988). Smear slides were prepared for this study to both confirm the lithologies and sample descriptions from the original core logs and also visually assess the nature and occurrence of green minerals in the sediment.

The nine samples listed above were prepared as smear slides using the method outlined by Marsaglia et al. (2013). A 1-2mm^3 portion of each sediment sample was scooped using the flat side of a toothpick, applied to a glass slide, and disaggregated using the toothpick and a few drops of Millipore water until it is thinly and evenly disseminated. The slurry was then dried on a hot plate for several minutes until the water evaporated. Once cooled, a few drops of Norland Optical Adhesive 61 (refractive index 1.56) was placed in the middle of the slide and a coverslip was gently applied to minimize bubbles. The slides were cured under a UV light until the adhesive had hardened. Completed slides were optically analyzed using a Zeiss Axioskop petrographic microscope and the components for each sediment sample were recorded.

Geochemical Analysis

All samples selected for smear slide preparation and analysis were also prepared for geochemical analysis based on procedures outlined by Murray et al. (2000). The bulk samples were first ground to a powder using an alumina mortar and pestle. The bulk sample powder was weighed to 100 mg, mixed with 400 mg of lithium metaborate flux, and added to graphite crucibles including one blank consisting of flux only. The flux mixtures were fused in a muffle furnace for 30 min at 1050ºC, then the heated bead was digested in 50 mL of 7% nitric acid.

Samples were magnetically stirred for 30 minutes until dissolved, then filtered into Nalgene bottles for a 500x diluted sample. 6.5 mL of each filtered sample was made up to 50mL using 2% nitric acid for a 4,000x dilution. A 10,000x dilution was prepared using 0.5 mL of the 500x solution made up to 10 mL with 2% nitric acid immediately prior to analysis.

Samples were analyzed with a Thermo Scientific iCap Q inductively-coupled plasma mass spectrometer (ICP-MS) for trace, major, and rare earth element data. Twelve previously-prepared United States Geological Survey (USGS) standards were included with the sample rack to track the instrument's calibration throughout its analysis: DNC-1, BHVO-2, G-2, W-2, BCR-2, GSP-2, QLO-1, AGV-2, SC0-1, BIR-1, RGM-1, and MAG-1. A drift solution was analyzed every five samples to check for variations in response intensity over the instrument's run time.

XRD Analysis

Four samples which had the highest observed glauconite in the smear slide analysis were analyzed using X-ray diffraction (XRD). For the first run, the powdered bulk samples were loaded into sample trays and analyzed using a Phillips X-PERT PRO X-ray diffractometer. Parameters were set at 45 kV, 40 mA, 0.02 step size with continuous scan at 1 second per step from 4 to 75 2θ, and CuKα radiation.

The mineral assemblage in the clay fraction of marine sediments depends greatly on the climatic conditions on land and the composition of surficial source rocks, and can therefore be a useful tool for paleoclimate reconstructions (Ehrmann et al., 1992). For the second analysis, four samples with the highest percentage of clay (<2 μm) as determined by the 2016 particle size analysis (Light, 2017) were selected for XRD analysis on the clay portion of the sediment. Oriented slide mounts of the clay particles were prepared using a modified method based on Brandt et al. (2013) and Moore and Reynolds (1997). Orienting clay particles is preferable for the analysis of phyllosilicates since it forces particles to lie flat, which allows the X-ray beam to be

directed down the minerals' z axis and detect basal diffractions which can be used in mineral identification (Poppe et al., 2001). Characteristic expansion and contraction of certain clay minerals can be observed along the z axis with a series of treatments including air drying, glycolation, heating to 400ºC, and heating to 550 ºC (Poppe et al., 2001).

Both Brandt et al. (2013) and Moore and Reynolds (1997) methods suggest removing carbonate content from a sample with a chemical treatment prior to separating the clay, however, the presence of carbonate in the sediment was assessed after hydrochloric acid treatment during the particle size analysis and was found to be negligible. Original smear slide records also suggest that minimal carbonate content is present in the sediment samples (Barker et al., 1988), therefore no chemical treatment was used in this study.

Approximately 1 cm^3 of each sample was added to a 250mL glass beaker with ~50mL of Millipore water and a small scoop of sodium pyrophosphate solid and sonicated for 20 minutes. The sediment solution was decanted into two 50 mL test tubes and filled with additional Millipore water. Test tubes were centrifuged at 1,000 rpm for 5 minutes to remove particles larger than 2μm, and the solution with suspended clay was decanted into clean test tubes. The remaining solution was centrifuged at 2,000 rpm for 15 minutes to remove the clay particles, and the sodium pyrophosphate solution was decanted off. To rinse the clay, it was resuspended in 50mL of Millipore water and again centrifuged at 2,000 rpm for 15 minutes. The rinse solution was decanted and clay was resuspended in 50mL of Millipore water until smear slides were prepared. The suspended clay solution was centrifuged at 2,000 rpm for 15 minutes a final time and decanted. The concentrated clay suspension was applied to glass slides using a dropper to evenly disperse the solution, and placed in an oven at 65ºC for approximately 30 minutes until dry.

Ethylene glycol treatment is used to expand swelling clays (e.g. montmorillonite, nontrolite, and beidellite) and provide additional information for XRD mineral identification (Poppe et al., 2001). Glycolated samples were prepared using the "slurry method" outlined by Novich and Martin (1983) to produce the maximum possible hydration of expandable layers

using the most reproducible technique. A small amount (~0.05g) of Miralax solid (polyethylene glycol 3350) was added directly to ~2.5mL of concentrated clay suspension. The glycolated mixture was applied to glass slides after 15 minutes and dried in a desiccator overnight.

Heat treatment can aid in identifying clay minerals by revealing crystal structure spacing changes due to collapsing expandable layers (Poppe et al., 2001). After they were analyzed, untreated slides were placed in the muffle furnace at 400ºC for two hours, analyzed on the XRD, then reheated at 550ºC for two hours to assess the change in 2θ peaks. Heat treatment was only carried out for two samples (56R-01W-5-7 and 56R-01W-125-127) since no peak shifting or significant collapse was observed in XRD spectra.

All slides were stored in the desiccator until immediately prior to XRD analysis to avoid rehydration. Clay slides were analyzed on the XRD with parameters set at 45 kV, 40 mA, 0.02 step size with continuous scan at 2 seconds per step from 4 to 30 2θ, and CuKα radiation.

Results

Smear Slides

The composition of the study samples was determined by optical analysis of the smear slides using guidance by Marsaglia et al. (2013). Results were recorded in an Excel template based on the Tool for Microscopic Identification (University of Minnesota, 2011) and are presented in Table 1.

Results of the smear slide sample analysis was generally consistent with initial on-board observations (Barker et al., 1988), which are presented in a similar format in Table 2. As the particle size analysis indicated, there is a fining upward trend in the estimated amounts of clay, silt, and sand over the late Eocene interval.

Green minerals were identified in all of the study samples in plane-polarized light, with 56R-01W-125-127, 56R-02W-88-90, 57R-01W-5-7, and 57R-01W-105-107 containing more than 30%. Individual crystals of these minerals could not be resolved optically, which indicates that, as expected, they are largely present in the clay fraction of the sediment. In the high glauconite samples, the clay is often clumped around other mineral grains. Quartz appears to be the dominant mineral in the silt and sand fraction, along with a smaller proportion of plagioclase feldspar. These silt and sand grains generally appear rounded. Trace amounts of calcium carbonate grains are present in most samples, and the lowermost sample, 58R-02W-55-58, contains mostly calcium carbonate sand grains.

Table 3 summarizes the selected sample depth, updated estimate of glauconite composition, and the estimated clay fraction determined by the smear slide analysis.

Table 1: Composition of smear slide study samples

core/ section	depth (mbsf)	TEXTURE	Sand %	Silt %	Clay %	COMPOSITION	Quartz	Feldspar	Rock fragments	Mica	Volcanic Glass	Accessory minerals	Glauconite	Opaque minerals	Amphiboles	Zeolites	Unidentified	Heavy Minerals	Nannofossils	Diatoms	comments
55R-06W-39-41	576.09		10	40	50		20	15	-	-	-		5	-	-	5	-	Tr	-	-	Mostly clay, some larger rounded quartz grains
56R-01W-5-7	577.95		10	20	70		10	5	-	-	-		30	5	-	Tr	-	-	-	-	Mud with organic material and silty glauconite
56R-01W-125-127	579.2		15	40	45		20	15	-	-	-		40	10	-	5	-	3	-	-	Glauconite mud with some grains of CaCO3 sand
56R-02W-88-90	580.28		10	50	30		20	10	-	Tr	-		45	3	-	2	-	Tr	-	-	Mostly glauconite, larger clumps surround darker rhombs, small particles of glauconite clay, rounded grains of plag and quartz, trace rounded grains of andalusite, small zeolite shards
57R-01W-5-7	587.65		15	60	25		25	10	-	-	-		40	5	-	15	-	Tr	-	-	Glauconite mud with some grains of CaCO3
57R-01W-105-107	588.65		20	50	30		20	10	-	Tr	-		40	10	-	5	-	-	-	-	Glauconite mud, some brown organic material
58R-01W-55-57	597.75		40	30	20		35	5	-	2	-		10	20	-	5	-	-	-	-	Some larger grains of CaCO3, coarse silt/very fine sand
58R-01W-87-89	598.07		50	30	20		30	10	-	-	-		3	30	5	1	-	-	-	-	Some larger grains of CaCO3
58R-02W-55-58	599.25		40	35	25		30	10	-	5	-		5	5	-	-	-	5	-	-	Some organic material, mostly CaCO3 sand

Tr: trace amounts present
- : not observed

Table 2: Composition of study samples as recorded on-board ODP Leg 113 (Barker et al., 1988)

core/ section	depth (mbsf)	TEXTURE	Sand %	Silt %	Clay %	COMPOSITION	Quartz	Feldspar	Rock fragments	Mica	Clay	Volcanic Glass	Accessory minerals	Glauconite	Opaque minerals	Amphiboles	Zeolites	Unidentified	Heavy Minerals	Nannofossils	Diatoms	comments
55R-06W-39-41	576.09		16	44	40		16	8	6	8	40	2		8	4	6	-	-	-	-	-	
56R-01W-5-7	577.95		20	50	30		19	4	2	-	30	6		20	4	-	15	-	-	-	-	
56R-01W-125-127	579.15		20	50	30		19	4	2	-	30	6		20	4	-	15	-	-	-	-	
56R-02W-88-90	580.28		20	60	20		19	6	2	2	20	4		45	-	-	2	-	-	-	-	
57R-01W-5-7	587.65		20	60	20		18	3	3	Tr	20	6		40	2	-	2	20	-	-	-	"Unidentified mineral which comprises 20-70% of the composition"
57R-01W-105-107	588.65		20	60	20		18	3	3	Tr	20	6		40	2	-	2	20	-	-	-	
58R-01W-55-57	597.75		25	50	25		42	4	-	2	25	-		20	3	1	-	-	3	-	-	coarse silt/very fine sand
58R-01W-87-89	598.07		10	20	70		10	-	-	5	70	1		2	3	1	-	-	1	3	-	coarse silt/very fine sand
58R-02W-55-58	599.25		50	24	26		30	10	-	3	26	3		15	5	3	-	-	5	1	Tr	coarse silt/very fine sand

Tr: trace amounts present
- : not observed

Table 3: Glauconite and clay estimates of study samples from smear slide observations

Sample ID	Depth (mbsf)	Glauconite (%)	Clay Fraction (%)
55R-06W-39-41	576.09	5	50
56R-01W-5-7	577.95	30	70
56R-01W-125-127	579.15	40	45
56R-02W-88-90	580.28	45	30
57R-01W-5-7	587.65	40	25
57R-01W-105-107	588.65	40	30
58R-01W-55-57	597.75	10	20
58R-01W-87-89	598.07	3	20
58R-02W-55-58	599.25	5	25

Geochemistry

Trace and major element intensities were translated into parts per million and weight-percent oxide (for majors) using an Excel spreadsheet that calculates calibrations for each element and accounts for drift and sample weights. R^2 values for all element calibrations exceeded 0.9 with the exception of Ga and Eu; these elements' R^2 values were below 0.7 and were not used in this study. Typically, the average of three runs on the ICP-MS is used to calculate sample results. However, an argon gas depletion occurred during the third run which significantly dropped the measured counts for the majority of the samples. Therefore, the results of only the first two runs were used to calculate sample concentrations. Concentrations determined by the ICP-MS analysis are included in the Appendix (Tables A-3, A-4, and A-5).

Elemental enrichments were calculated by dividing the concentrations determined by ICP-MS by the average elemental concentrations in the upper continental crust (Rudnick and Gao, 2014). Separate diagrams were also created for the four samples with high observed glauconite (>30%) and the five remaining samples for comparison.

Major Elements

All samples showed major element oxide depletions of Al_2O_3 and (to a lesser extent) TiO_2 (see Figures 13-15). Most samples, with the exception of the deepest (58R-2W-55-58),

showed depletions of MnO, CaO, Na_2O, and P_2O_5 (Figure 13). Samples with high observed glauconite (Figure 14) showed enrichments of Fe_2O_3 and K_2O and generally more significant depletions of TiO_2, Al_2O_3, CaO, and Na_2O. Sample 58R-2W-55-58 had large enrichments in MnO, and CaO unlike the other samples in this study. The smear slide analysis of 58R-2W-55-58 observed significant calcium carbonate grains present in this sample, so the high calcium value for this sample is likely a result of $CaCO_3$ rather than a higher component of calcium present in the silicate fraction.

K_2O concentrations were plotted with Al_2O_3 (see Figure 16) to determine any changes in detrital clays relative to background Al (Sageman and Lyons, 2003). High observed glauconite samples (highlighted by the green box) showed distinctly higher K_2O/Al_2O_3 ratios when compared to low glauconite samples.

Several major element indices were calculated after Robert and Maillot (1990) to determine sedimentation conditions:

$Mn^* = \log (MnO \text{ sample}/MnO \text{ average upper crust})/(Fe \text{ sample}/Fe \text{ average upper crust})$

$D = Al_2O_3/(Al_2O_3+Fe_2O_3+MnO)$

$Si^* = SiO_2/Al_2O_3$

Upper crust averages from Rudnick and Gao (2014) are used. Mn* variations relate to influences from volcanism and/or oxidizing currents (Robert and Maillot, 1990). Since Al_2O_3 is generally conservative in minerals, the D index shows the terrigenous detrital influence on sedimentation; a D value less than 0.63 indicates a less significant detrital fraction (Robert and Maillot, 1990). High values of Si* show additional silicate contribution from volcanic, biogenic, or detrital sources (Robert and Maillot, 1990). Sediment samples overall exhibit low Mn* values (between -0.5 and -1.2), with the exception of the lowermost sample 58R-02W-55-58 where Mn* = 1.1. D index values were notably lower for high-glauconite samples (0.2-0.5); other sample D index values were between 0.6-0.7. No similar trend was observed in Si* values, which generally ranged from 6-10 with higher values of 13 at 55R-06W-39-41 and 18 at 57R-01W-105-107. A

summary of major element indices downcore is presented in Figure 17 and Table A-1 in the Appendix.

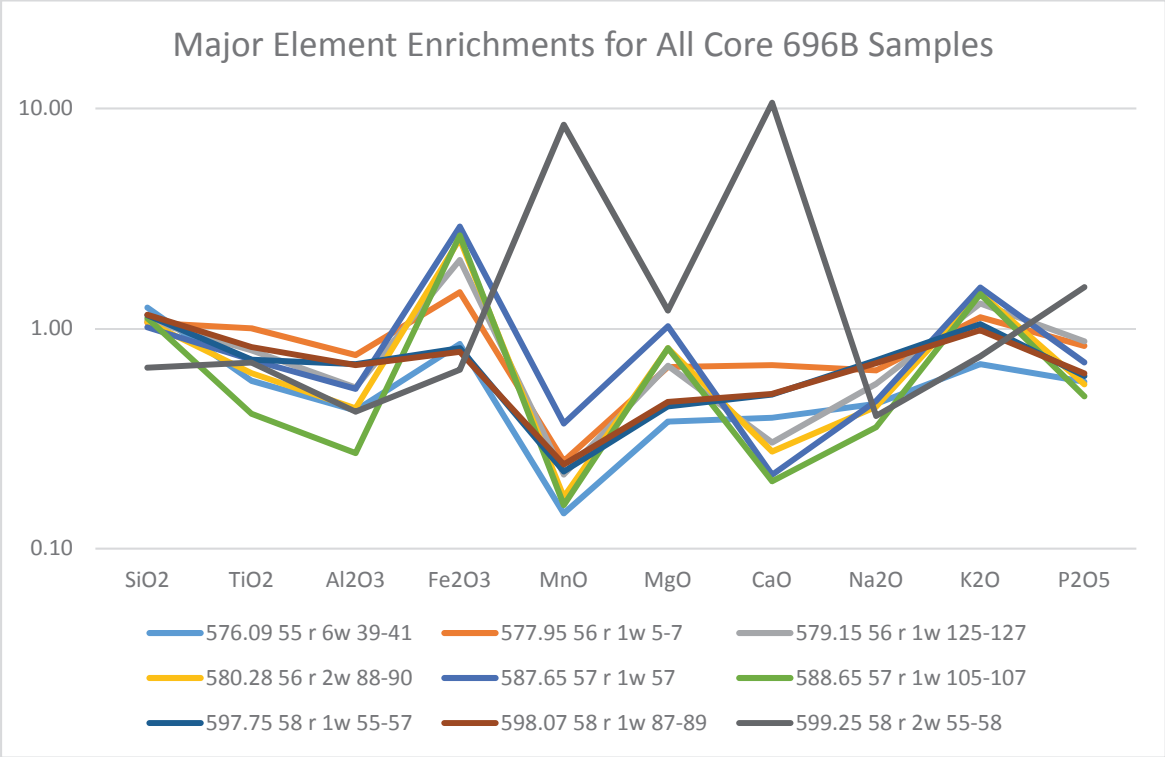

Figure 13: Major element enrichments relative to average upper continental crust values (Rudnick and Gao, 2014); values above 1 indicate enrichment and values below 1 indicate depletion.

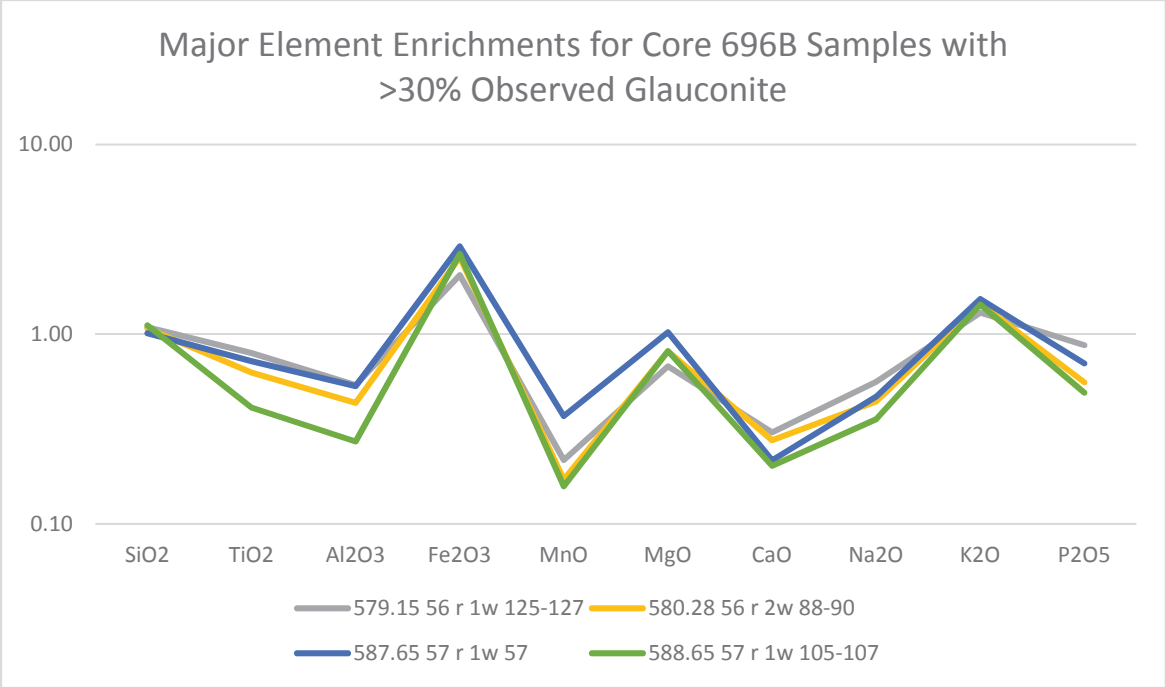

Figure 14: Major element enrichments relative to average upper continental crust values (Rudnick and Gao, 2014) for study samples with more than 30% observed glauconite

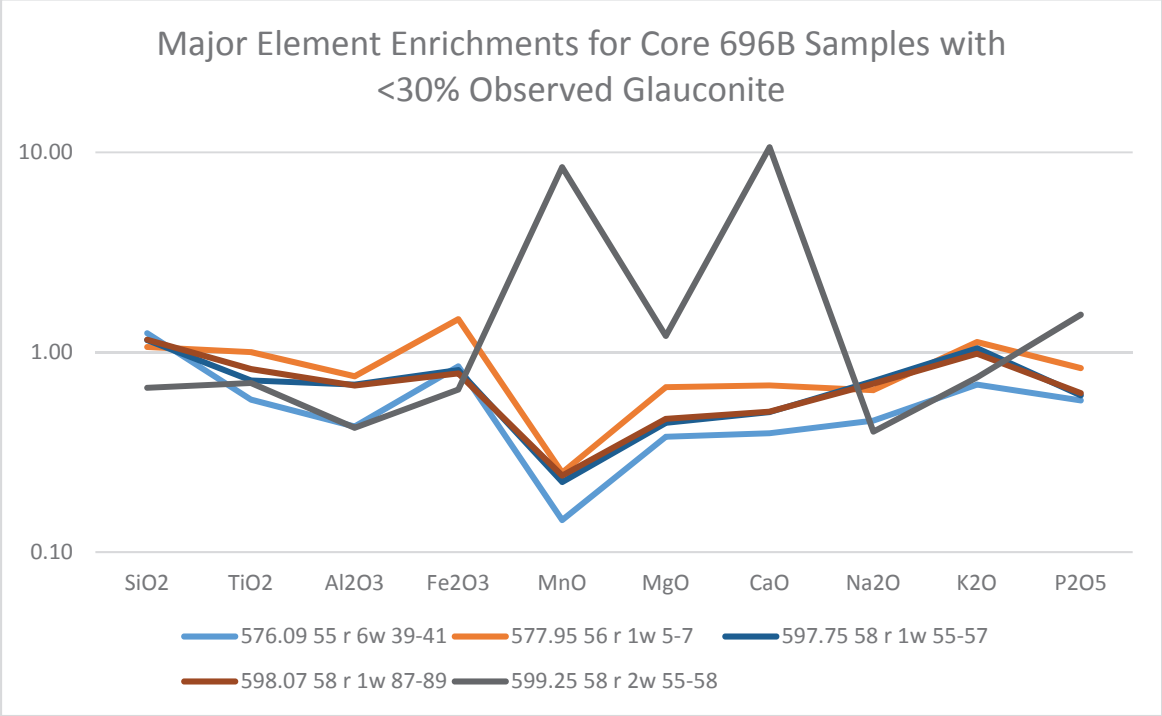

Figure 15: Major element enrichments relative to average upper continental crust values (Rudnick and Gao, 2014) for study samples with less than 30% observed glauconite

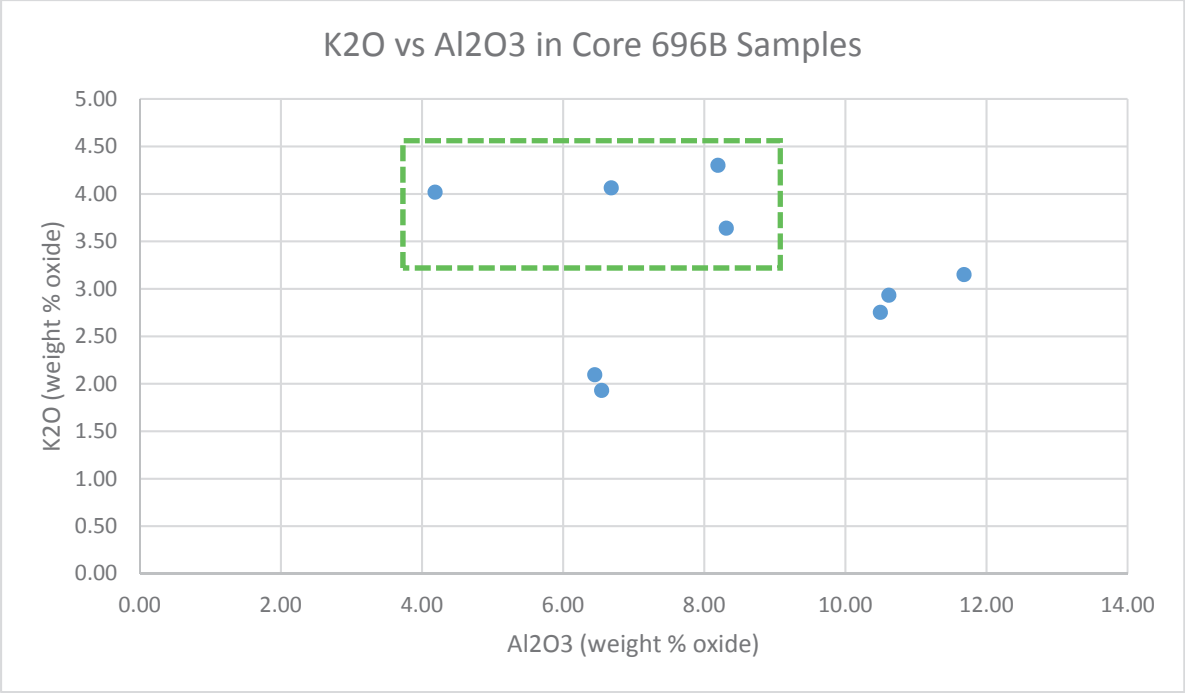

Figure 16: K_2O concentrations plotted with Al_2O_3 in weight percent oxide. The green box indicates high glauconite (>30%) samples.

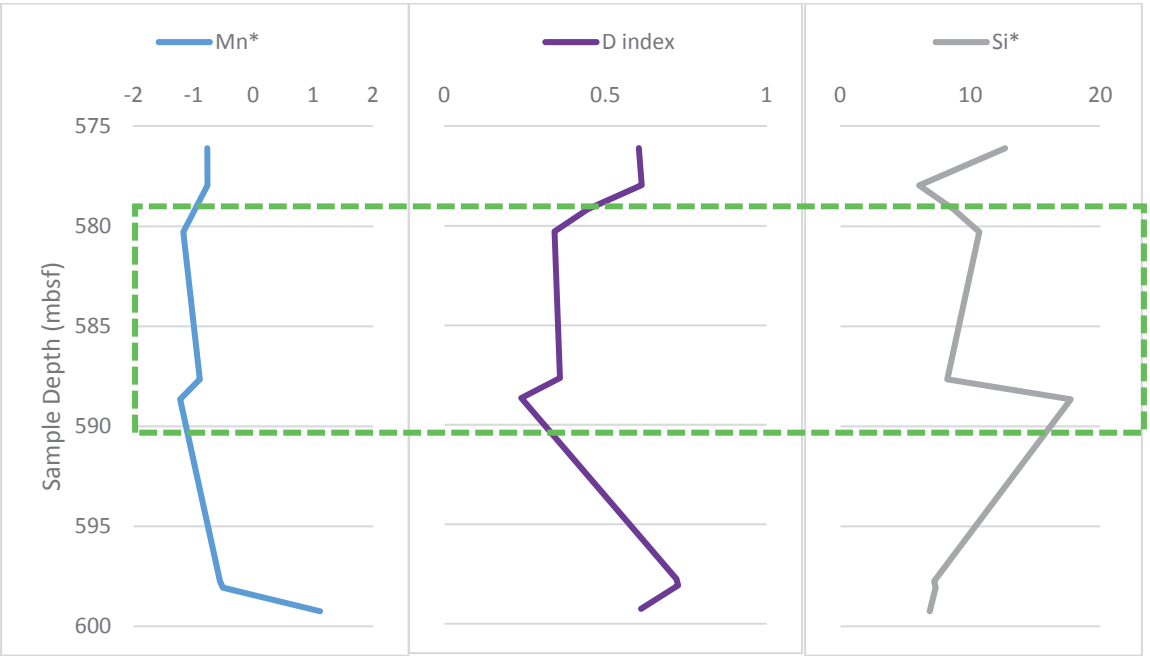

Figure 17: Major element indices in study samples. Green box indicates high-glauconite (>30%) sample interval)

Trace Elements

Trace element analysis revealed depletions of Co, Ni, and Pb for all samples (see Figures 18-20). High observed glauconite samples showed an enrichment in Cr and Cs compared to the lower observed glauconite samples which showed a slight depletion. Samples that contained lower observed glauconite showed an enrichment in Ba relative to the high glauconite samples, yet all samples showed an overall slight Ba depletion from the average continental crust values. All samples showed a depletion of Sr, with the exception of 58R-2W-55-58 which had a slight enrichment. High observed glauconite samples also showed more significant depletion in Sr compared to the lower glauconite samples.

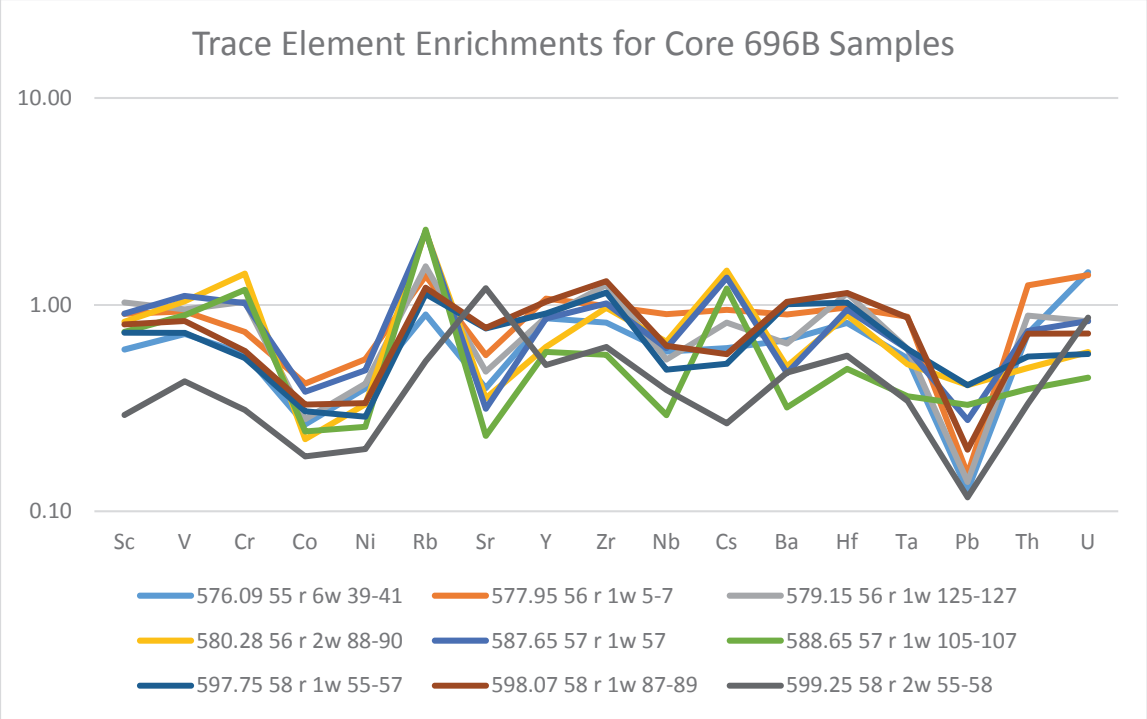

Figure 18: Trace element enrichments relative to average upper continental crust values (Rudnick and Gao, 2014) for study samples

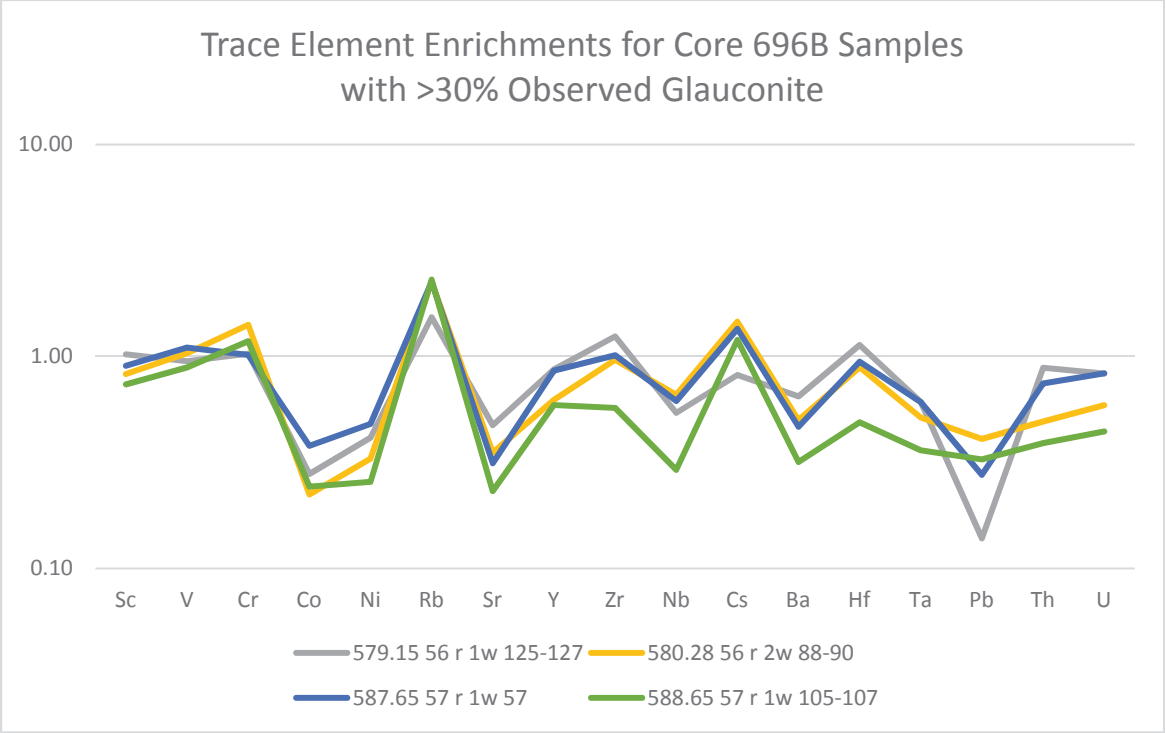

Figure 19: Trace element enrichments relative to average upper continental crust values (Rudnick and Gao, 2014) for study samples with more than 30% observed glauconite

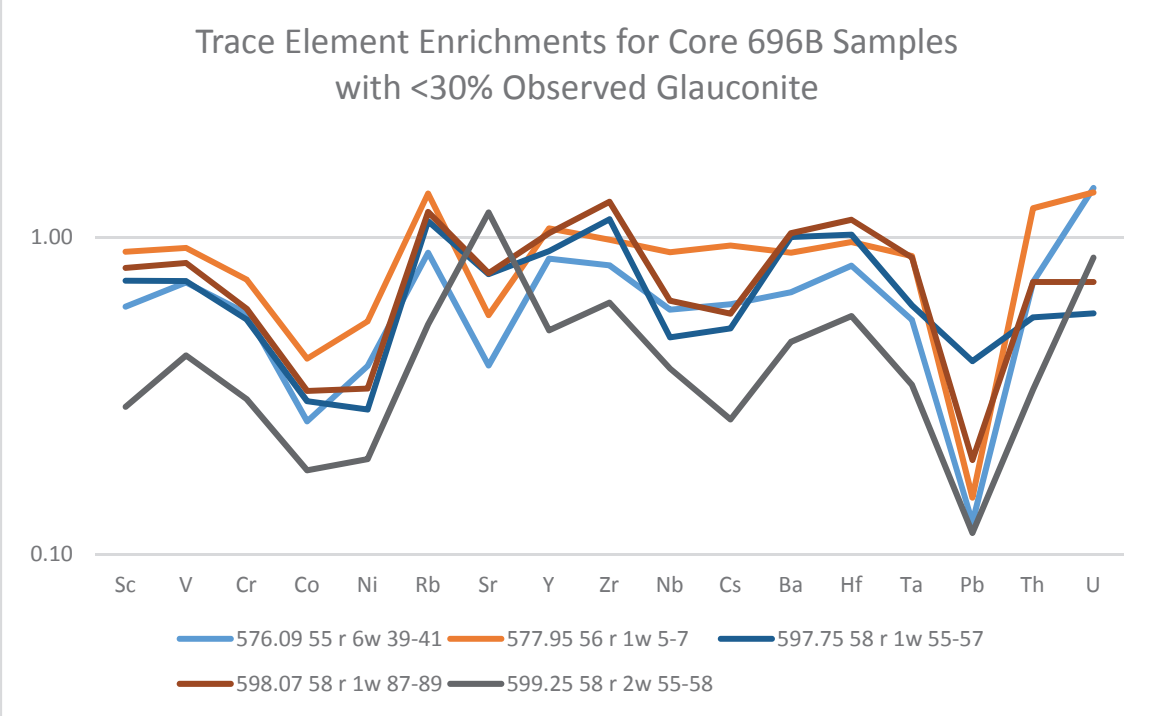

Figure 20: Trace element enrichments relative to average upper continental crust values (Rudnick and Gao, 2014) for study samples with less than 30% observed glauconite

Rare Earth Elements

Rare earth elements (REEs) did not vary significantly from average upper crust values compared to trace and major element data; the study samples generally showed slight depletions (see Figures 21-23). High observed glauconite samples are depleted in all REEs, and depletion appears to slightly increase with sample depth. Samples with low observed glauconite also generally show slight depletions. The 56R-01W-5-7 and 58R-01W-87-89 samples are exceptions, which have REE enrichments close to 1 and are slightly enriched with Sm, Gd, and Tm. The lower-most sample, 58R-02W-55-58, is the most significantly depleted of all REEs.

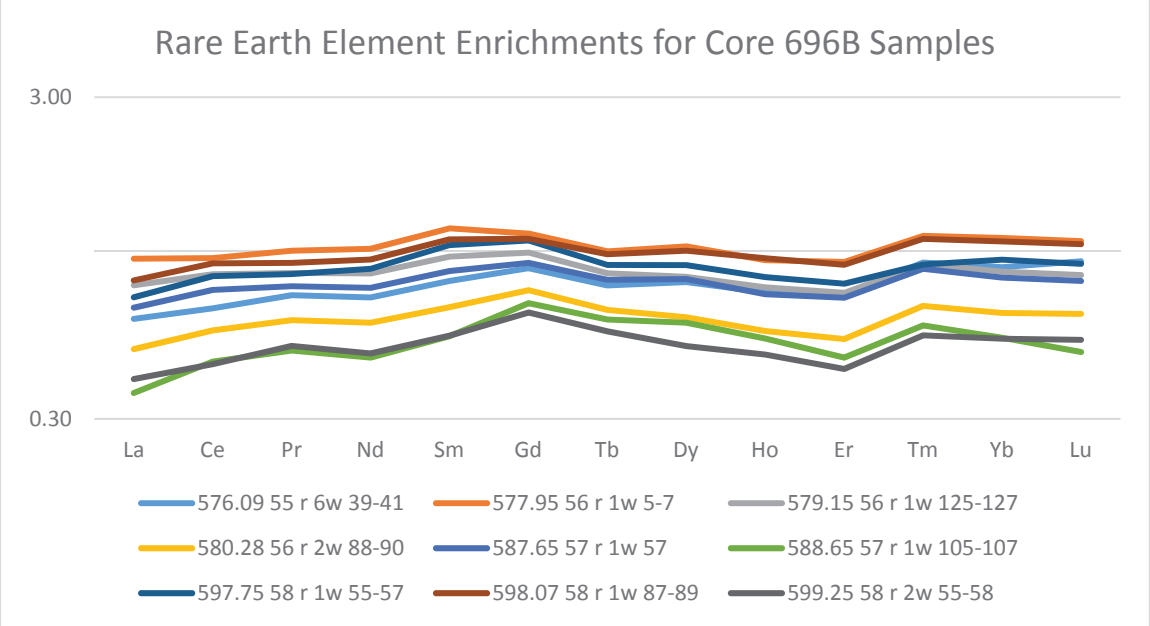

Figure 21: Rare earth element enrichments relative to average upper continental crust values (Rudnick and Gao, 2014) for study samples

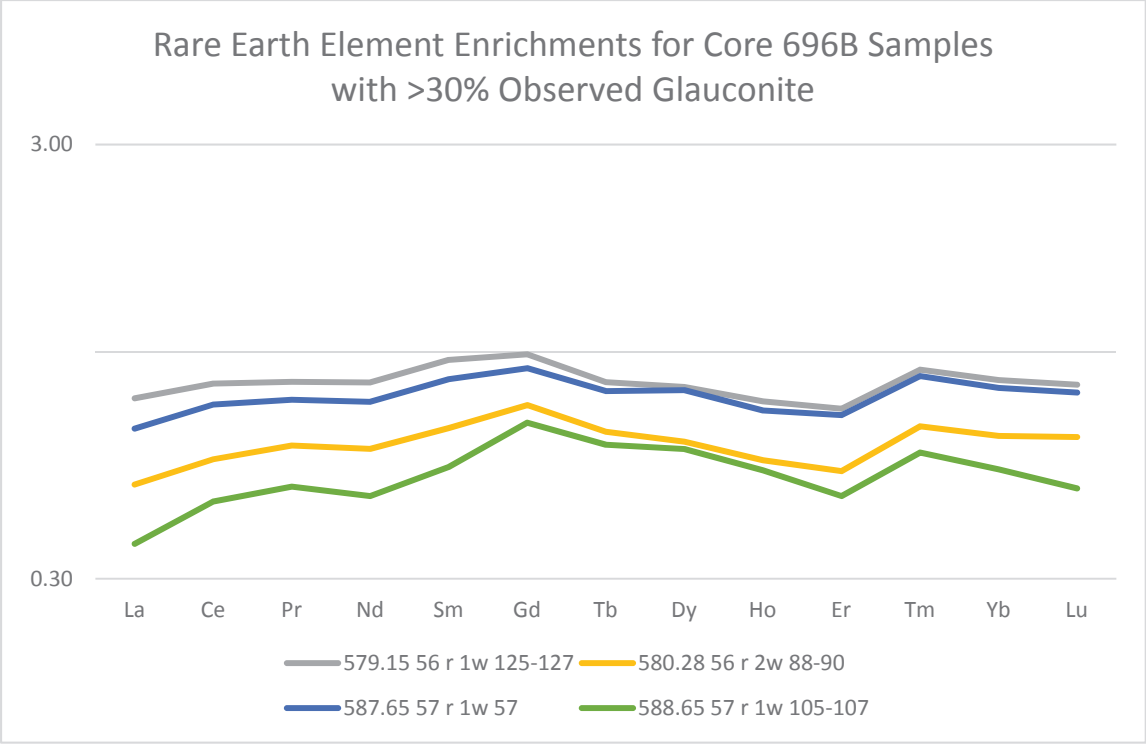

Figure 22: Rare earth element enrichments relative to average upper continental crust values (Rudnick and Gao, 2014) for study samples with more than 30% observed glauconite

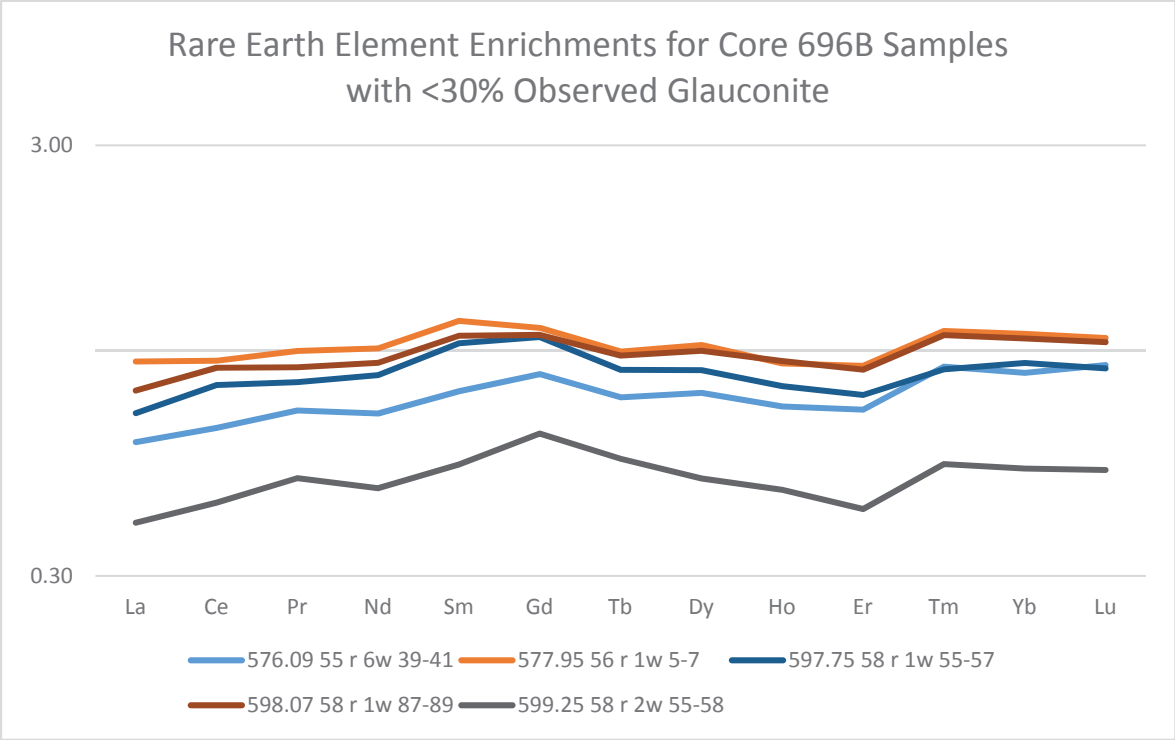

Figure 23: Rare earth element enrichments relative to average upper continental crust values (Rudnick and Gao, 2014) for study samples with less than 30% observed glauconite

Redox-Sensitive Elements

Downcore trends of redox-sensitive elements (V, Cr, Co, Ni, U, Mn, and Fe) were also examined relative to Ti and Al, which are conservative elements representative of the terrigenous detrital sediment fraction (Shaw et al., 1990 and Sageman and Lyons, 2005). By normalizing concentrations with respect to Ti and Al, observable elemental enrichments or depletions are a result of authigenic mineral precipitation or dissolution that occurs in response to changing redox conditions on the sea floor.

Trends for both elemental normalizations over the study interval were similar (see Figures 24 and 25). Concentrations of Ti and Al-normalized V, Cr, Mn, and Fe were significantly enriched in the authigenic sediment fraction of high glauconite samples (between ~579-590 mbsf) compared to the lower glauconite samples located above and below this interval (with the exception of the lower-most sample 58R-02W-55-58). Ti- and Al-normalized U, Ni, and Co remained relatively stable downcore. Mn was more than an order of magnitude more enriched in $CaCO_3$-cemented 58R-02W-55-58. This trend suggests a transition throughout the core interval to a more reducing, suboxic environment during the period in which glauconite formed in the sediment. The stability of Ni and Co also indicates a reducing environment since these elements are often precipitated with MnO, then remobilized into pore water under suboxic conditions (Shaw et al., 1990).

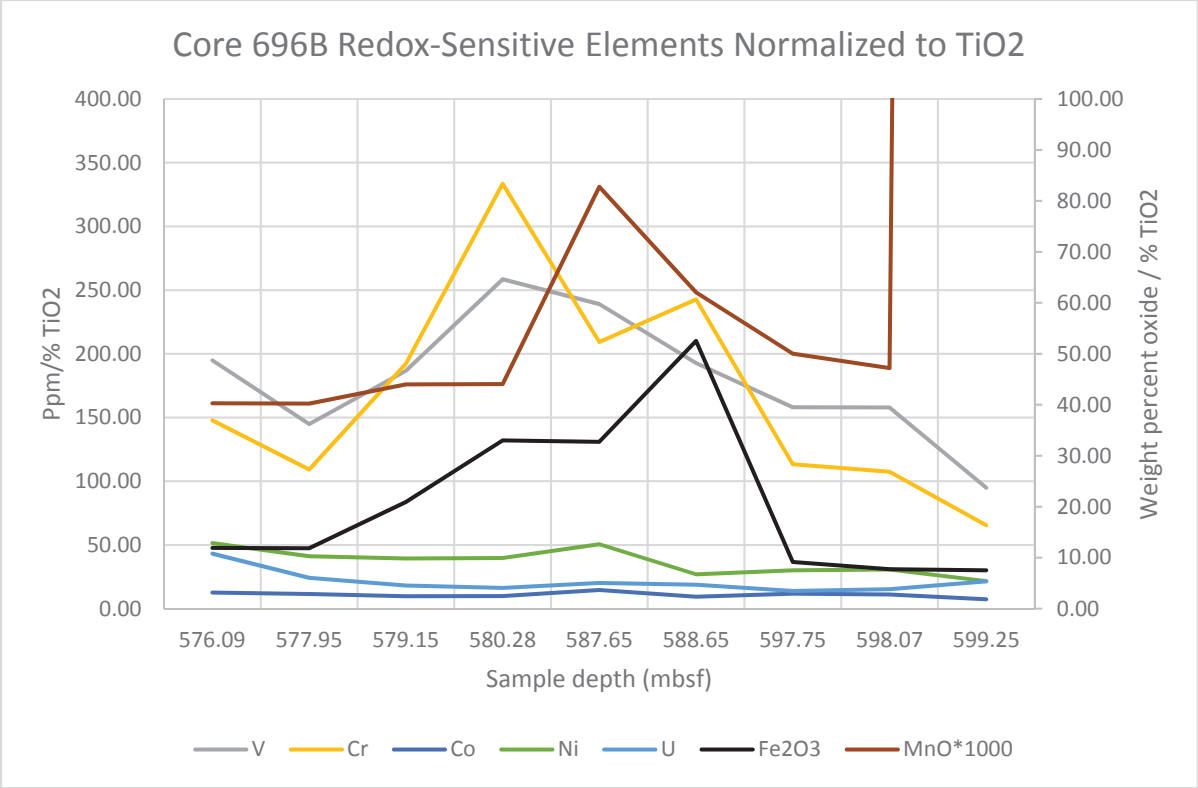

Figure 24: Redox-sensitive elemental enrichments normalized to TiO_2 sample concentrations. Major elements (Fe_2O_3 and MnO) are plotted on the right axis as weight percent oxide, which omits the maximum concentration of MnO for clarity.

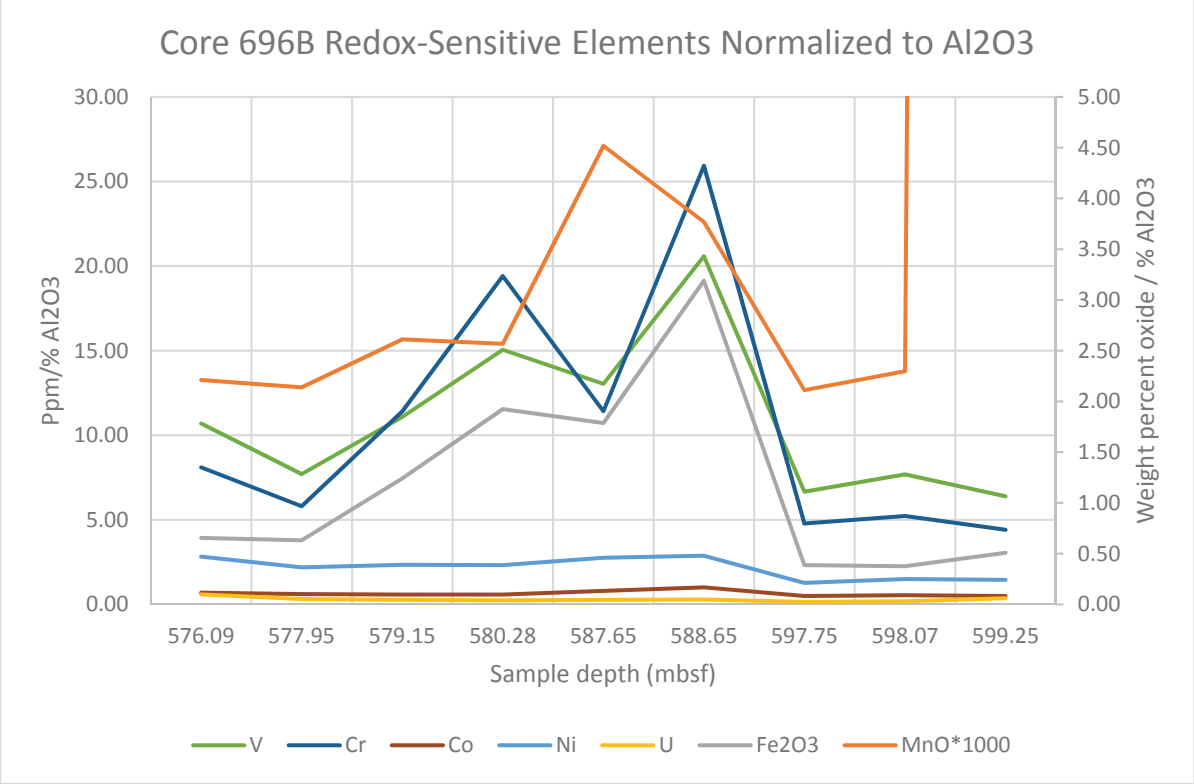

Figure 25: Redox-sensitive elemental enrichments normalized to Al_2O_3 sample concentrations. Major elements (Fe_2O_3 and MnO) are plotted on the right axis as weight percent oxide, which omits the maximum concentration of MnO for clarity.

XRD

Bulk sample XRD results were analyzed and processed using the Phillips XPERT High Score software. Background noise was removed and K-alpha 2 was stripped prior to matching peaks with a library of known minerals. Results of bulk powder XRD analysis are shown in Figures 26-30. High Score peak matching results are included in the Appendix (Figures A-1 through A-4).

Quartz was the dominant mineral detected by High Score for the four samples analyzed. No peaks at 2θ angles characteristic of clay minerals were observed; they were likely obscured by the sharp, high intensity peaks from quartz and plagioclase feldspar.

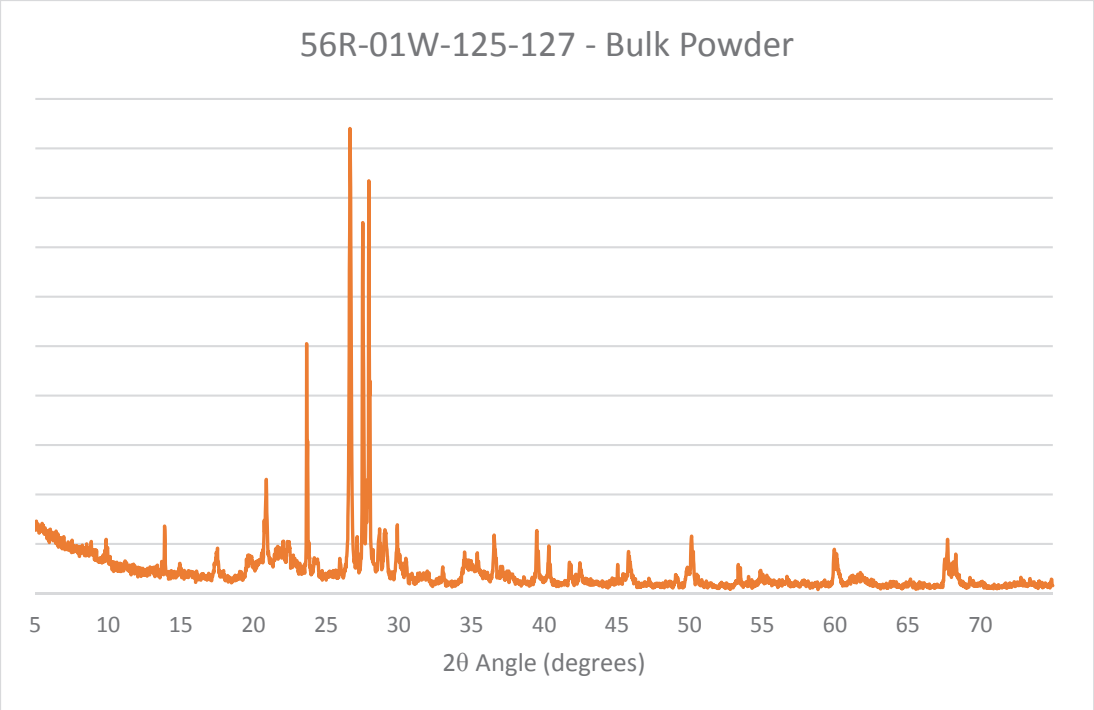

Figure 26: XRD analysis of the 56R-01W-125-127 powdered bulk sample

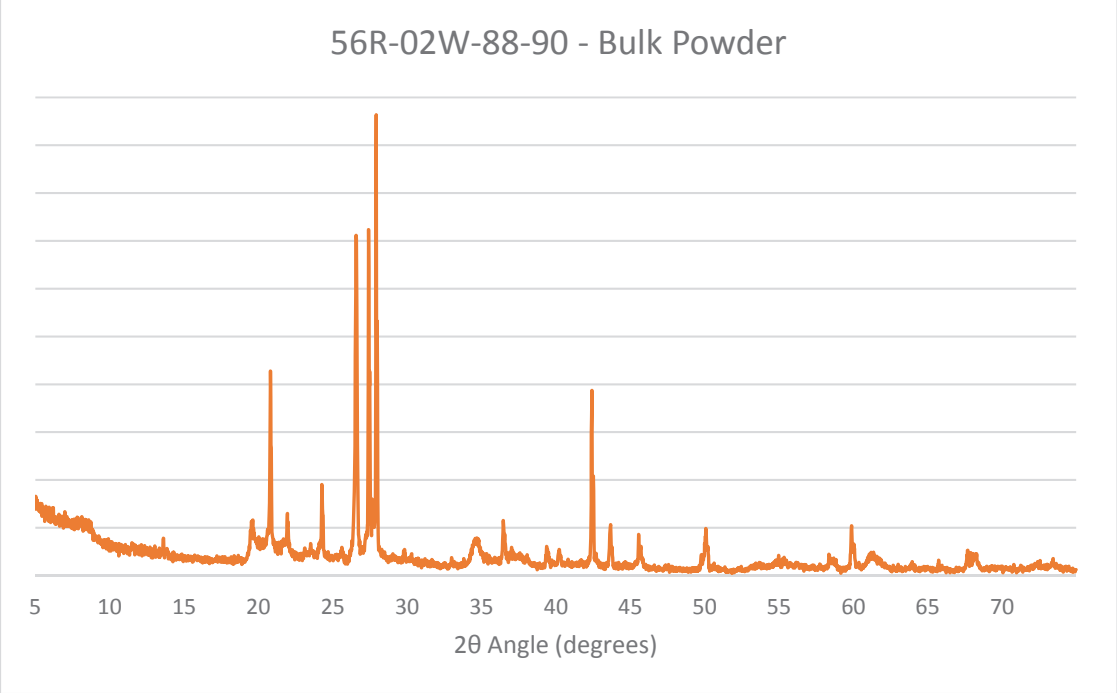

Figure 27: XRD analysis of the 56R-02W-88-90 powdered bulk sample

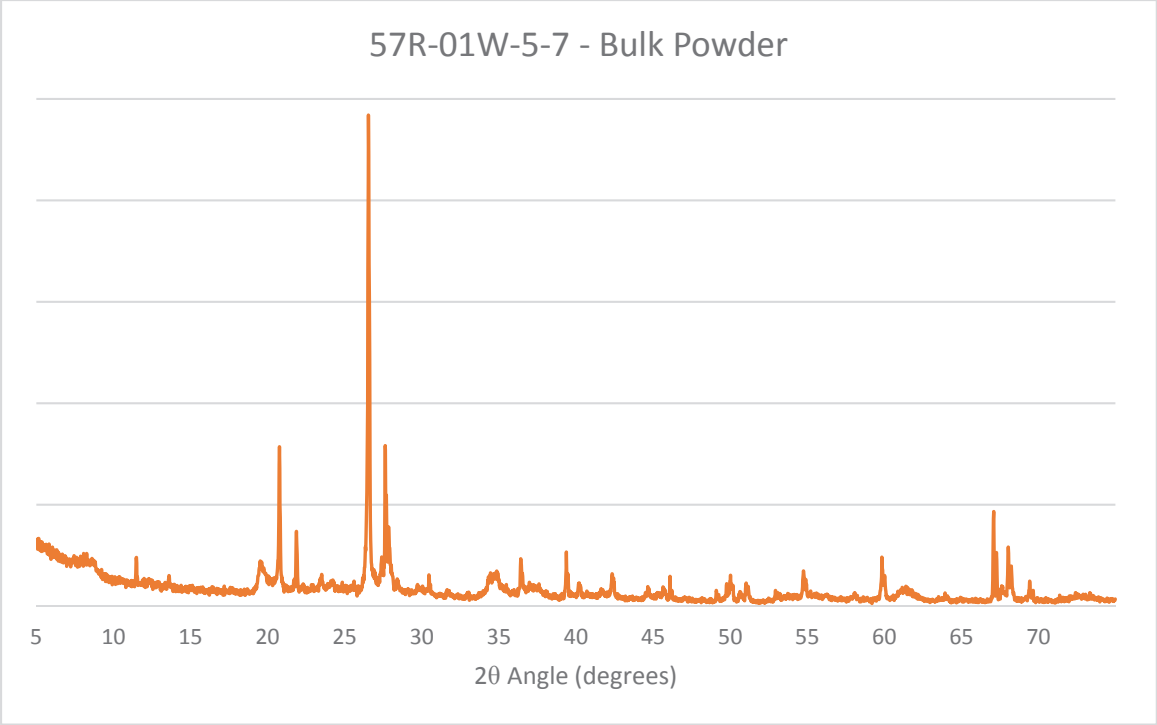

Figure 28: XRD analysis of the 57R-01W-5-7 powdered bulk sample

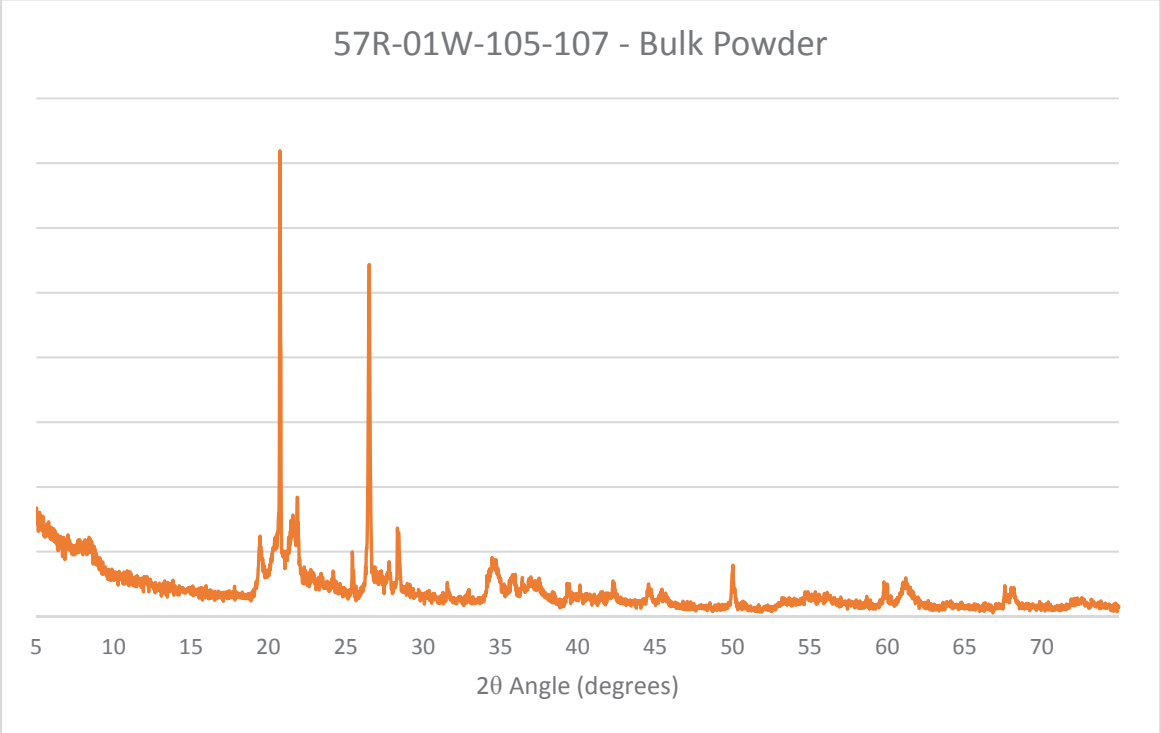

Figure 29: XRD analysis of the 57R-01W-105-107 powdered bulk sample

Detected counts from the clay slide samples were much lower than the corresponding bulk powder results, and no data processing was performed. Results of XRD analysis of the clay slides are shown in Figures 30-33.

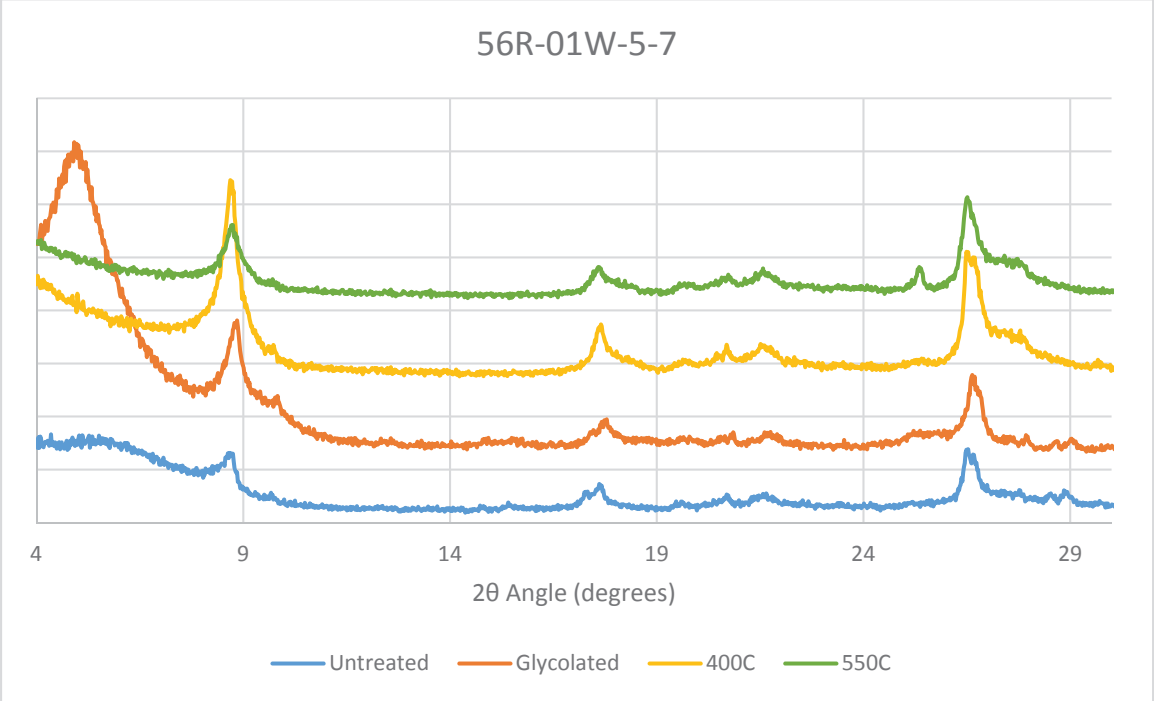

Figure 30: XRD analysis of clay (<2µm) fraction from sample 56R-01W-5-7. Intensities of glycolated and heat-treated runs are off-set for visibility.

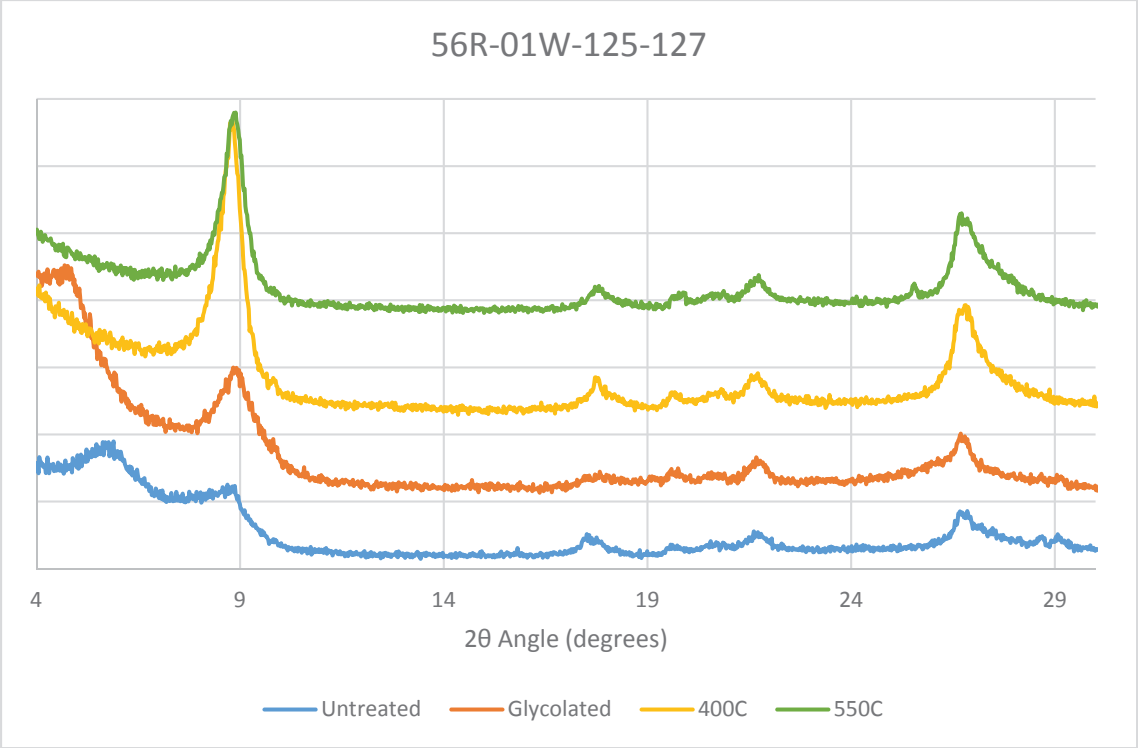

Figure 31: XRD analysis of clay (<2µm) fraction from sample 56R-01W-125-127. Intensities of glycolated and heat-treated runs are off-set for visibility.

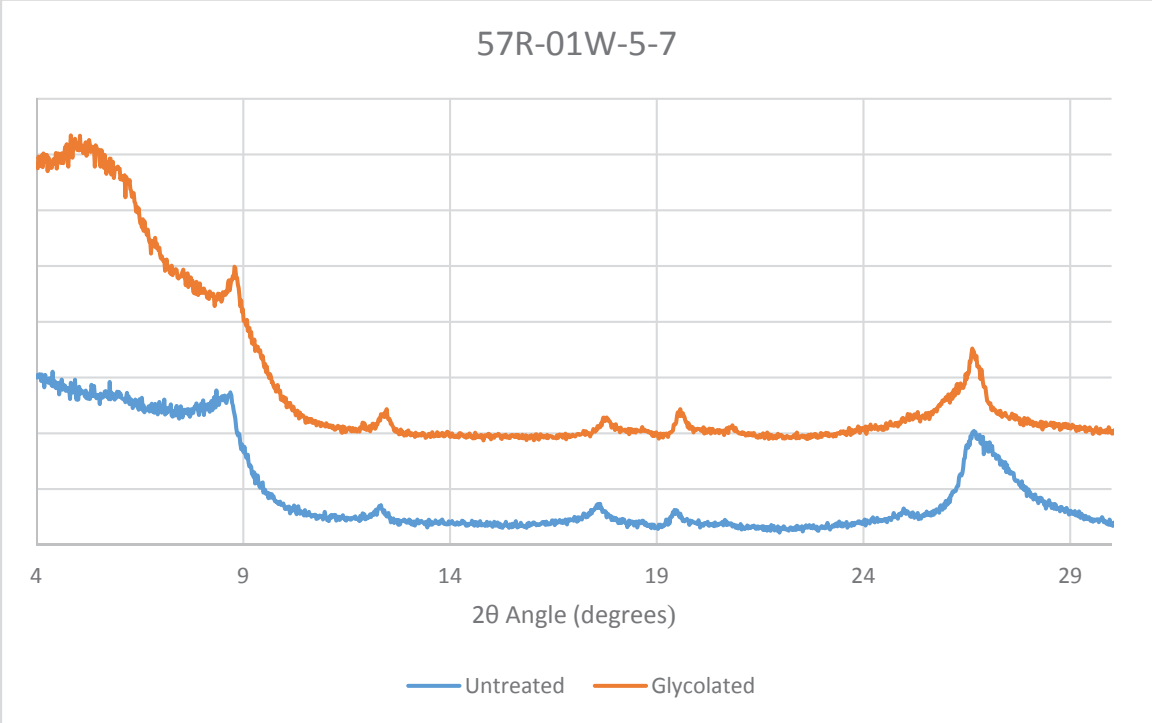

Figure 32: XRD analysis of clay (<2µm) fraction from sample 57R-01W-5-7. Intensities of the glycolated run are off-set for visibility.

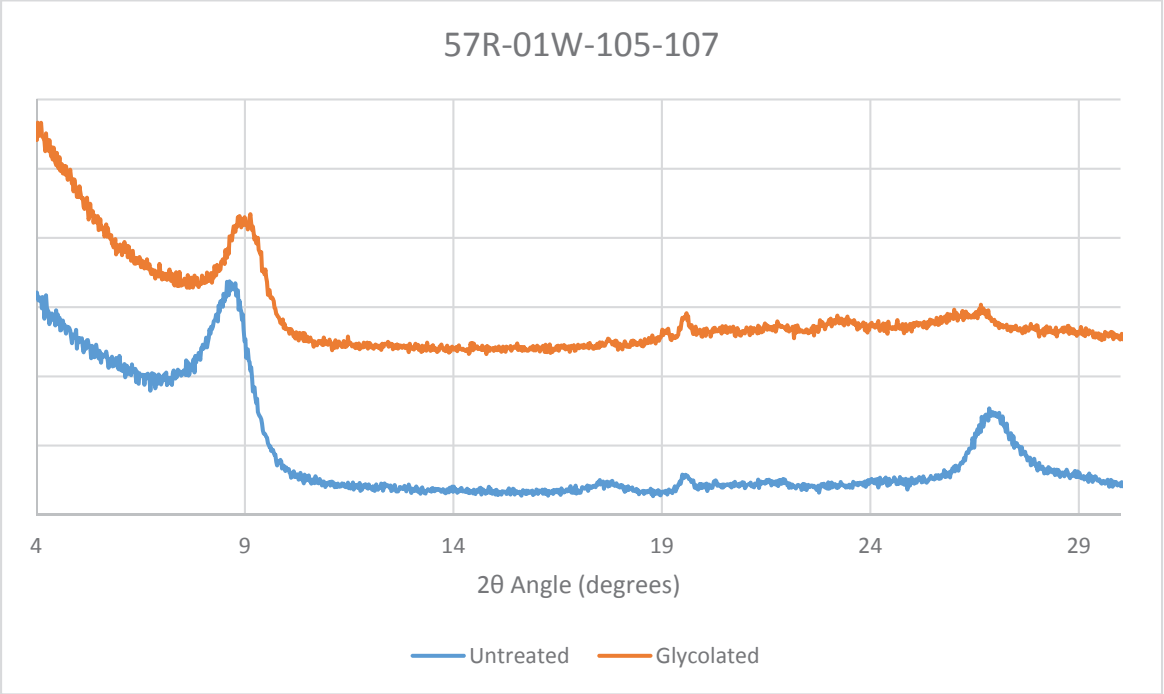

Figure 33: XRD analysis of clay (<2µm) fraction from sample 57R-01W-105-107. Intensities of the glycolated run are off-set for visibility.

XRD data from the clay samples was reviewed using the USGS Clay Mineral Identification Flow Diagram (Poppe et al., 2001) and Velde's (2005) classification schema of green clay minerals. Compared to the bulk powder XRD spectra, the peaks observable in the clay samples are much broader, with lower overall detectable counts. The largest peak for all of the untreated clay samples occurs at 8.8º, or a d-spacing of ~10 Å. A second significant peak occurs in each sample at 26.7º, at a d-spacing of ~3.3 Å. Both the 10 Å and 3.3 Å peaks were unaffected by treatment with ethylene glycol and heating at 400ºC and 550ºC. Each sample also includes a broad hump or shoulder from 4-8º, which corresponds to a d-spacing of 11-22 Å. Minor peaks also occur at 12.5º, 17.7º, 19.7º, 20.7º, and 21.8º in different spectra as outlined in Table 4.

Table 4: Summary of clay sample XRD results

d spacing (Å)	2θ (degrees)	56R-01W-5-7	56R-01W-125-127	57R-01W-5-7	57R-01W-105-107
18	4.9	G	G	G	-
15	5.9	u	U	-	-
10	**8.8**	**X**	**X**	**X**	**X**
7	13	-	-	x	-
5	18	-	x	x	x
4.5	20	-	x	-	-
4.3	21	x	-	-	-
4.1	22	x	x	-	-
3.3	**27**	**X**	**X**	**X**	**X**

G: peak only observed in sample treated with ethylene glycol
u: small peak only observed in untreated sample
U: large peak only observed in untreated sample
X: large peak observed in all (untreated, glycolated, and heat-treated) samples
x: small peak observed in all samples
-: peak not observed at d-spacing/2θ value

A peak at 4.9º (~18 Å) appears upon glycolation in three samples, two of which contain a slight peak in the untreated sample at 5.9º (~15 Å). It is possible that the third sample with a peak at 4.9º also has a response at 5.9º in the untreated sample that is obscured by background noise and the shoulder from 4-8º. The 5.9º peaks in the untreated samples collapse with heat treatment at 400ºC. No effects are observed with additional heating at 550ºC. These high d-spacing peaks are due to the presence of a smectite component, likely montmorillonite, which has an 001 reflection ~14 Å that swells with glycolation. The 001 reflection of smectite collapses to 10 Å with heating, which coincides with the most significant peak at 8.8º. As a result, the 10 Å peak shows a marked increase with heating for the samples that had a corresponding 001 smectite peak in the untreated and glycolated samples.

Of all clay minerals, only the illite group is characterized by intense 10 Å 001 and 3.3 Å 003 peaks that are unaffected by ethylene glycol and heating to 550ºC (Poppe et al., 2001). Glauconite is differentiated from illite by a weak (or lack of a) 5 Å peak, as shown in Figure 34 (Moore and Reynolds, 1997). While a 5 Å peak is present in most samples, it is very weak and barely distinguishable from background noise, therefore the dominant 10 Å and 3.3 Å peaks can be attributed to glauconite, with additional contribution to the 10 Å peak from collapsed smectite layers.

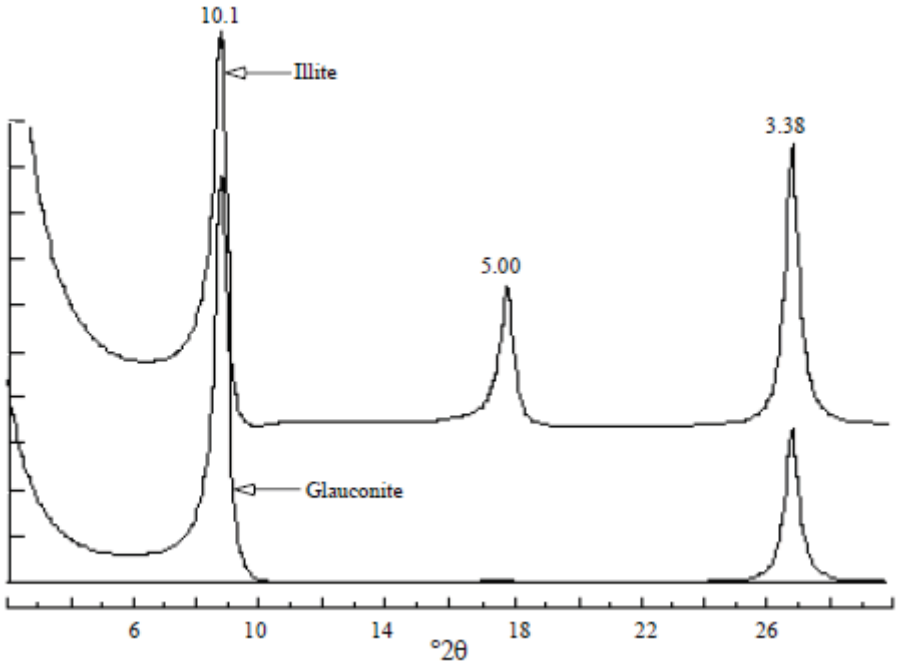

Figure 34: Calculated XRD patterns for illite and glauconite using NEWMOD program (Moore and Reynolds, 1997)

Discussion

Smear Slides

Glauconite typically forms as pellets in sedimentary rock (Velde, 2005; Amorosi, 1997; McRae, 1972), but no individual pellets were observed in hand samples used in this study. Smear slides largely confirmed original on-board sediment composition estimates made by Barker et al. (1988). Optical analysis showed that grains of the green mineral are amorphous and largely present in the clay fraction of the sediment, though often clumped together around larger grains. Particle size analysis by Light (2017), however, determined significantly less clay present in the study samples than the amount of glauconite observed. This could indicate that a portion of the nascent glauconite forms on the surface of silt-sized particles. Odin and Matter (1981) suggest that parent material for glauconite formation is most commonly carbonate particles, but the lack of carbonate observable in the high-glauconite samples indicates that the formation mechanism is more likely alteration of degraded clay.

Geochemistry

Major element results indicate significant enrichments of potassium and iron in high-glauconite samples, which is consistent with additional sediment contribution from authigenic glauconite. Low D index values also suggest authigenic mineral precipitation and a reduced detrital input over the high-glauconite interval. Low Mn* index values indicate that, with the exception of the lowermost sample 58R-02W-55-58, sediment was deposited in a reducing environment; high glauconite samples had the most negative Mn* values. Chromium and vanadium, other elements indicative of reducing conditions (Shaw et al, 1990), are also elevated in high-glauconite samples. These results suggest that sediment was formed in deeper waters that were not subject to oxidizing currents or significant detrital input.

Such sedimentary conditions could be caused by a local sea level rise and an increase in organic material and benthic biological activity, contributing to increased glauconite formation (Moore and Reynolds, 1997). The Site Report recorded evidence of strong bioturbation over 56R and 57R (Barker et al., 1988), but very few organisms were available for biostratigraphic analysis. Some organic material was observed in smear slides, though not at significantly higher amounts over the high-glauconite interval.

Geochemical results of the lowermost sample in this study (58R-02W-55-58) are anomalous relative to the other samples analyzed. The Mn* index indicates the presence of oxidizing currents, precipitation of Mn-carbonates, and a transition to suboxic conditions after approximately 35.4 mya.

Few glauconite studies to-date have conducted comparable trace elemental and REE analyses; those that exist were conducted on highly-evolved glauconite pellets. Bansal et al. (2018) found a “hat-like” pattern of REE in glauconite samples from Cretaceous sedimentary rock. No such pattern of REE was observed in samples from this study, which points to a more incipient form of the mineral. Jarrar et al. (2000) found no consistent relationship between trace and major element patterns, and REE concentrations to be lithologically-controlled. Trace elements were found to not be true structural components of the glauconite itself, rather they were adsorbed onto the surface of glauconite grains or substrate remnants (Jarrar et al., 2000). Therefore, the patterns of enrichment and depletion observed for trace elements in this study can be attributed to the percentage of authigenic material present in the sediment relative to the detrital component and effects of grain-size partitioning (Light, 2017 and Lepp, 2018).

Clay Minerals

XRD analysis confirms that the green mineral is glauconite with a minor presence of expandable smectite in the clay fraction of sediment samples. The broad shape of the XRD peaks

in the untreated samples suggests a nascent or slightly evolved form of the mineral (see Figure 35 below). This supports the smear slide results which showed the glauconite present as small, amorphous grains, as well as geochemistry results.

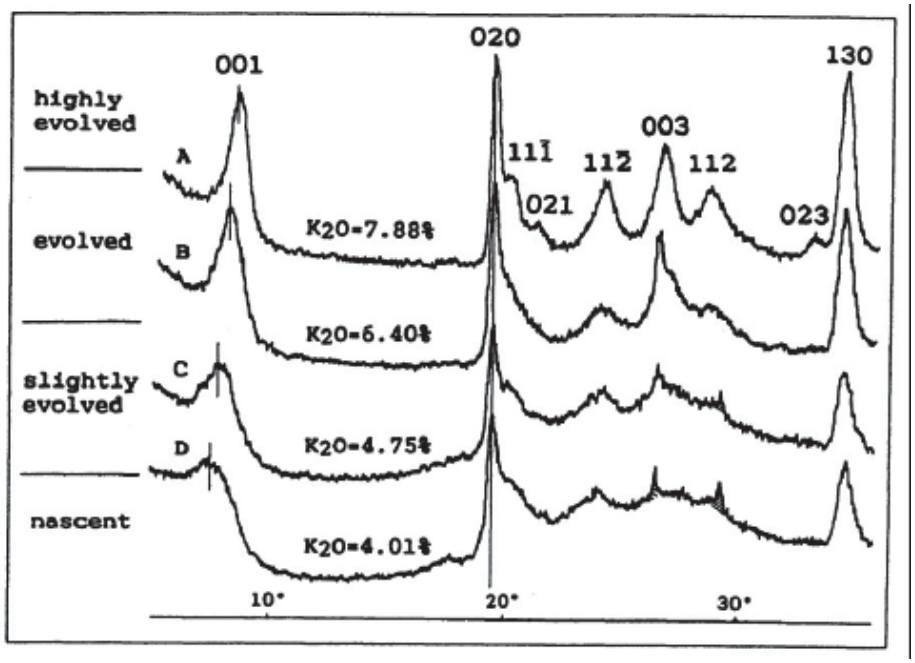

Figure 35: XRD patterns of glauconite at different stages of evolution (Amorosi, 1997)

Results also confirm the low-resolution clay mineral study by Robert and Maillot (1990), which found mud from sample 57R-1 to be mainly authigenic. Deconnick et al. (1988) determined that transformation from smectite to glauconitic illite in Purbeckian carbonates resulted from repeated wetting and drying cycles in a shallow tidal environment; Robert and Maillot (1990) concluded the formation of the glauconite-rich interval in core 696 also occurred near-shore. The results of this study, however, suggest that it is more likely that the sediment was deposited at-depth with low sedimentary disturbance. The presence of detrital quartz grains and the lack of carbonates in the glauconite-rich interval support this scenario. Despite the variable depositional conditions in which glauconite has been found, it is generally considered to be one of the most sensitive indicators of low sedimentation rate in marine environments (Amorosi, 1997).

Illite and associated mixed layer clays are derived from poorly-developed soils or erosion of the parent rock; they indicate predominantly physical weathering conditions in which clay minerals cannot further evolve (Diester-Haass et al., 1993). XRD results confirm geochemistry results by Light (2017) from East Antarctica which suggested a reduced rate of chemical weathering resulting from low temperatures and rainfall in the late Eocene; this was found to continue up-core at Site 696 as the transition to the Oligocene progresses (Lepp, 2018). Increasing illite in clay mineral assemblages has also been observed over EOT intervals from East Antarctica (Diester-Haass et al., 1993; Robert and Maillot, 1990). In Site 689 (also from ODP Leg 113) EOT samples, sediments from less productive periods were found to generally contain more illite (Diester-Haass, et al., 1993), while more productive periods contain more smectite. No evidence of kaolinite was found, which would be indicative of chemical weathering under extremely warm and humid climates (Ehrmann and Mackensen, 1992). The smectite peaks from glycolated clay samples visible on XRD spectra is likely montmorillonite, a common alteration product of feldspar in an alkaline environment, as would be found on the ocean floor (Carroll, 1970).

The significant and abrupt glauconization of sediment over the study interval indicates a shift to more reducing, low sedimentary conditions during the cooling temperate waters and ice sheet advance of the late Eocene at Site 696. These conditions were likely caused by a relative sea level rise, and glauconite is particularly associated with marine transgressions (Odin and Matter, 1988; McRae, 1972). Particle size analysis over the EOT interval contained sequentially finer particles, which is consistent with a relative sea level rise (Light, 2017). A marine transgression under a cooling climate is likely due to crustal subsidence from the weight of an advancing continental ice sheet, as has been modelled for East Antarctica (Stocchi et al., 2013). Glauconite mineralization is highest over the 56R-57R core interval, indicating this change was most significant around ~34.5-35 mya.

A local increase in ocean productivity caused by early calving of icebergs could have also contributed to the increase in reducing conditions and iron and organic matter concentrations, prompting glauconite formation, as illustrated in Figure 36. Carter et al. (2017) found that most of the larger grains deposited at Site 696 during the late Eocene originated from ice-rafted debris, therefore icebergs were a significant mode of transport for sediment, leading to likely increases of phytoplankton productivity and chlorophyll. In addition to the transport and deposition of sediment grains, icebergs have enhanced primary productivity within a few kilometers in the Weddell Sea, similar to estuaries supplying nutrients to coastal regions (Smith et al., 2007 and Duprat et al. 2016).

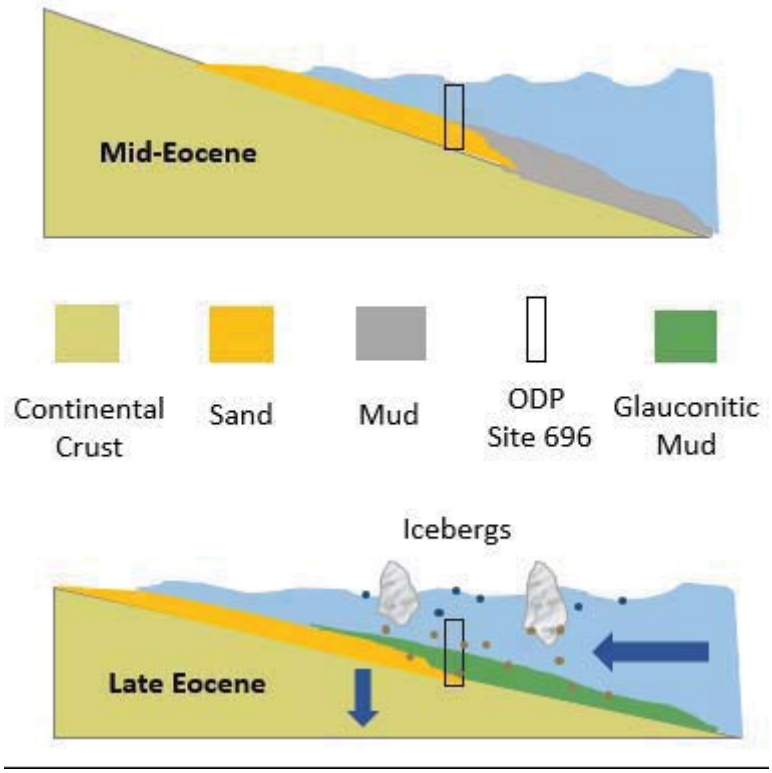

Figure 36: Conceptual site model for ODP Site 696 over the study interval. Crustal subsidence leading to a marine transgression likely promoted glauconite formation in late Eocene sediment. Sediment formation was also likely influenced by icebergs, providing both ice-rafted debris and localized productivity.

Nutrient blooms supplied by calving and seasonal glacial ice changes would have affected the productivity of SOM waters and sediment formation long before the establishment of a continental-scale ice sheet (Houben et al., 2013). The provenance of sand grains attributed to ice-rafted debris in the EOT interval shows both the East Antarctic margin of the Weddell Sea and the Ellsworth-Whitmore mountains in West Antarctica are sediment sources (Carter et al., 2017). It is unclear however, if ice-rafting was the dominant mode of transport from both sources, or if other oceanic processes were involved (Carter et al., 2017). Further complicating the interpretation of Site 696 EOT interval, the provenance of 55R sediment deposited from 34.3-33.5 mya was recently attributed to mainly local SOM sources (Lepp, 2018). It is possible that the influence of icebergs on sediment in the SOM region was restricted to the late Eocene prior to a sea level decrease at the onset of the early Oligocene, but additional research is needed to further develop the model for Antarctic glacial advance.

Conclusions

This study investigated late Eocene climatic deterioration and its effects on West Antarctic mineralogy and geochemistry at ODP Site 696 using multiple analytical methods. Smear slide and XRD results show the dominant clay mineral over the green interval is an authigenic, low crystalline form of glauconite. Significant non-detrital contribution to the sediment load is evident from geochemistry results, with glauconite formation favored under more reducing conditions. The bulk sediment with high glauconite concentrations, as expected, is strongly enriched with iron and potassium

The abrupt shift from illite to glauconite as the dominant clay mineral in the study interval is caused by 1) a temperate climate resulting from cooling in the late Eocene, 2) a reduction in the rate of sedimentation, and 3) an increase in reducing sediment conditions, possibly catalyzed by a localized increase in ocean productivity. The high glauconite sediment over cores 56R-57R is evidence for a marine transgression in the South Orkney Microcontinent region during the late Eocene period, peaking between 34.5 and 35 mya. Uniquely high glauconite concentrations suggest that the impact of a marine transgression on the clay mineral assemblage was more significant at Site 696 relative to other ODP locations. These results document evidence for ice sheet advance prior to the EOT onset 34 mya and establishment of continental-scale glaciation.

Further Research

This study analyzed whole-sediment geochemistry, but additional analysis of K_2O in the glauconite fraction would show how evolved the mineral was relative to literature values (Amorosi, 1997; Odin, 1988), though sample volume could be a limitation. Scanning electron microscopy may also be a useful technique to gain more information on the texture of the glauconite grains if they are separated from the bulk sediment. To investigate the potential

contribution of localized productivity, a high-resolution comparison of the benthic foraminifera and organic content between high glauconite deposits in the EOT could be conducted to look for similarities or sudden changes. An investigation of 59R-62R samples at the base of Site 696 would show if the significant calcite and manganese present in Section 58R-02W and the implications for oxidizing currents is unique, or occurs over a larger interval and document any changes in the mid-late Eocene sediment leading up to these samples.

References

Amorosi, A., 1997, Detecting compositional, spatial, and temporal attributes of glaucony: a tool for provenance research, Sedimentary Geology, v. 109, p. 135-153.

Anderson, J. A., 1999, Antarctic Marine Geology, Cambridge University Press, New York, 289pp.

Bansal, U., Banerjee, S., Ruidas, D. K., and Pande, K., 2018, Origin and geochemical characterization of the glauconites in the Upper Cretaceous Lameta Formation, Narmada Basin, central India: Journal of Palaeogeography, v. 7, issue 2, p. 99-116.

Barker, P.F., Kennett, J. P., and Shipboard Scientific Party, 1988, Site reports Leg 113, Shipboard Scientific Party: Proceedings of the Ocean Drilling Program (ODP) Initial Reports.

Barker, P. F., Kennett, J. P., and Scientific Party, 1988, Weddell Sea Palaeoceanography: Preliminary Results of ODP Leg 113: Palaeogeography, Palaeoclimatology, Palaeoecology, v. 67, p. 73-102.

Brandt, L., Barnes, H., and Bronk, K., 2013, XRD: Quick User Guide, International Ocean Discovery Program, https://rosetta.iodp.tamu.edu/A/TechDoc/7006?encoding=UTF-8 accessed May 1, 2018

British Antarctic Survey, 2018, Bedmap2 – Ice thickness and subglacial topographic model of Antarctica, https://www.bas.ac.uk/project/bedmap-2/, accessed September 3, 2018.

Bryant, W. R. and Rack, F. R., 1990, 17. Consolidation characteristics of Weddell Sea sediments: Results of ODP Leg 113: Proceedings of the Ocean Drilling Program, Scientific Results, v. 113, p 211-223.

Carroll, Dorothy, 1970, Clay Minerals: A Guide to Their X-ray Identification, The Geological Society of America, Special Paper 126, Boulder, CO, 80pp.

Carter, A., Riley, T. R., Hillenbrand, C-D., and Rittner, M., 2017, Widespread Antarctic glaciation during the Late Eocene: Earth and Planetary Science Letters, v. 458, p. 49-57.

Chafetz, H., 2007, Paragenesis of the Morgan Creek Limestone, Late Cambrian, central Texas: Constraints on the formation of glauconite: Deep Sea Research II. v. 54, p. 1350-1363.

Chafetz, H. S. and Reid, A., 2000, Syndepositional shallow-water precipitation of glauconitic minerals: Sedimentary Geology, v. 136, p. 29-42.

Cloud, P., 1955, Physical Limits of Glauconite Formation: American Association of Petroleum Geologists Bulletin, v. 39 issue 4, p. 484-492.

Coxall, H. K., Wilson, P. A, Pällke, H., Lear, C. H., and Backman, J., 2005, Rapid stepwise onset of Antarctic glaciation and deeper calcite compensation in the Pacific Ocean: Nature, v. 433, p. 53-57.

Deconnick, J. F., Strasser, A., and Debrabant, P., 1988, Formation of Illitic Minerals at Surface Temperatures in Purbeckian Sediments (Lower Berriasian, Swiss and French Jura): Clay Minerals, v. 23, p. 91-103.

Diester-Haass, L., Robert, C., and Chamley, H., 1993, Paleoceanographic and paleoclimatic evolution in the Weddell Sea (Antarctica) during the middle Eocene-late Oligocene, from a coarse sediment fraction and clay mineral data (ODP Site 689): Marine Geology, v. 114, p. 233-250.

Duprat, L. P. A. M., Bigg G. R., and Wilton, D. J., 2016, Enhanced Southern Ocean marine productivity due to fertilization by giant icebergs: Nature Geoscience, v. 9, issue 3, pp. 219-221.

Ehrmann, W. U. and Mackensen, A., 1992, Sedimentological evidence for the formation of an East Antarctic ice sheet in Eocene/Oligocene time: Palaeogeography, Palaeoclimatology, Palaeoecology, v. 93 issues 1-2, p. 85-112.

Ehrmann, W. U., Melles, M., Kuhn, G., and Grobe, H, 1992, Significance of clay mineral assemblages in the Antarctic Ocean: Marine Geology, v. 107, issue 4, p. 249-273.

Force, E. R. and Cannon, W. F., 1988, Depositional model for shallow-marine manganese deposits around black shale basins: Economic Geology, v. 83 issue 1, p. 93-117.

Francis, J. E., Marenssi, S., Levy, R., Hambery, M., Thorn, V. T., … and DeConto, R., 2009, "From Greenhouse to Icehouse – the Eocene/Oligocene in Antarctica," Developments in Earth and Environmental Sciences, Elsevier B. V., v. 8, p. 309-368

Galeotti, S., DeConto, R., Naish, T., Stocchi, P., Florindo, F., … and Zachos, J. C., 2016, Antarctic Ice Sheet variability across the Eocene-Oligocene boundary climate transition: Science, v. 352, p. 76-80.

Houben, A. J. P., Bijl, P. K., Pross, J., Bohaty, S. M., Passchier, S., … and the Expedition 318 Scientists, 2013, Reorganization of Southern Ocean Plankton Ecosystem at the Onset of Antarctic Glaciation: Science, v. 340, p. 341-344.

Hugget, J., 2013, "Minerals: Glauconites and Green Clays," Reference Module in Earth Systems and Environmental Sciences, Elsevier, 7 pp.

Hugget, J., Adetunji, J., Longstaffe, F., and Wray, D., 2017, Mineralogical and geological characterization of warm-water shallow-marine glaucony from the Tertiary of the London Basin: Clay Minerals, v. 52, p. 25-50.

Ireland, J., Curtis, C. D., and Whiteman, J. A., 1983, Compositional variation within some glauconites and illites and implications for their stability and origin, Sedimentology, v. 30, p. 769-786.

Jarrar, G., Armireh, B., and Zachmann, D., 2000, The major, trace and rare earth element geochemistry of glauconites from the early Cretaceous Kurnub Group of Jordan: Geochemical Journal, v. 34, p. 207-222.

Kennett, J. P., 1977, Cenozoic evolution of Antarctic glaciation, the circum-Antarctic Ocean, and their impact on global paleoceanography: Journal of Geophysical Research, v. 82 issue 27, 3842-3860.

Lea, D. W., 2006, "Elemental and Isotopic Proxies of Past Ocean Temperatures," Treatise on Geochemistry, Elsevier Ltd., v. 6, p. 365-390.

Lee, H. M., Lee, J. I., Lee, M. J., Kim, J., and Choi, S. W., 2012, The A-type Pirrit Hills Granite, West Antarctica: an example of magmatism associated with the Mesozoic break-up of the Gondwana supercontinent: Geosciences Journal, v. 16 no. 4, p. 421-433.

Lepp, A. P., 2018, Geochemical and Sedimentological Analysis of Marine Sediments from ODP Site 696 and Implications for the Onset of Antarctic Glaciation, Montclair State University Theses, Dissertations, and Culminating Projects, 140.

Light, J. J., 2017, Geochemical and Particle Size Analysis of East Antarctic Shelf Sediments Through the Eocene Oligocene Transition, Montclair State University Theses, Dissertations, and Culminating Projects, 15.

Marsaglia, K., Milliken, K., and Doran, L., 2013, Integrated Ocean Drilling Program (IODP) Digital Reference for Smear Slide Analysis of Marine Mud: Part 1 Methodology and atlas of siliclastic and volcanogenic components, IODP Technical Note 1.

McRae, S. G. 1972, Glauconite: Earth-Sci. Rev., v. 8, p. 397-440.

Miller, K. G., Sugarman, P. J., Browning, J. V., Kominz, M.A., Olsson, R. K., … and Hernandez, J. C., 2004, Upper Cretaceous sequences and sea-level history, New Jersey Coastal Plain: GSA Bulletin, v. 116, p. 368-393.

Moore, D. M. and Reynolds, R. C., 1997, X-ray diffraction and the identification of clay minerals, Oxford University Press, 378p.

Murray, R.W., Miller, D.J., and Kryc, K.A., 2000, Analysis of major and trace elements in rocks, sediments, and interstitial waters by inductively coupled plasma–atomic emission spectrometry (ICP-AES): ODP Technical Note 29.

Novich, B. E. and Martin, R. T., 1983, Solvation methods for expandable layers: Clays and Clay Minerals, 31, p. 123-129.

Odin, G. S., 1988, Introduction to the Study of Green Marine Clays: Developments in Sedimentology, v. 45, p. 1-3.

Odin, G. S. and Matter, A., 1981, De glauconiarum origine: Sedimentology, v. 28, p. 611-641.

Pagani, M., Zachos, J. C., Freeman, K. H., Tipple, B., and Bohaty, S., 2005, Marked Decline in Atmospheric Carbon Dioxide Concentrations During the Paleogene: Science, v. 309, p. 600-603.

Poppe, L. J., Paskevich, V. F., Hathaway, J. C., and Blackwood, D. S., 2001, A Laboratory Manual for X-Ray Powder Diffraction, U. S. Geological Survey Open-File Report 01-041, Woods Hole, MA, 88p.

Prothero, D. R., 1994, The Eocene-Oligocene Transition: Paradise Lost, Columbia University Press New York, 283p.

Robert, C. and Maillot, H., 1990, 5. Paleoenvironments in the Weddell Sea Area and Antarctic Climates, as Deduced from Clay Mineral Associations and Geochemical Data, ODP Leg 113, Proceedings of the ODP, Scientific Results, 113.

Rudnick, R. L. and Gao, S., 2014, “Composition of the Continental Crust,” Treatise on Geochemistry, Elsevier Ltd., v. 4, p. 1-51.

Sageman, B. B. and Lyons, T. W., 2003, “Geochemistry of Fine-grained Sediments and Sedimentary Rocks,” Treatise on Geochemistry, Elsevier Ltd., v. 7, p. 115-158.

Shaw, T. J., Gieskes, J. M., and Jahnke, R. A., 1990, Early diagenesis in differing depositional environments: The response of transition metals in pore water, Geochimica et Cosmochimica Acta, v. 54, p. 1233-1246.

Smith, K. L., Robison, B. H., Helly, J. J., Kaufmann, R. S., Ruhl, H. A… and Vernet, M., 2007, Free-Drifting Icebergs: Hotspots of Chemical and Biological Enrichment in the Weddell Sea: Science, v. 317, p. 478-482.

Stocchi, P., Escutia, C., Houben, A. J. P., Vermeersen, B. L. A., Bijl, P. K., … and IODP Expedition 318 Scientists, 2013, Relative sea-level rise around East Antarctica during Oligocene glaciation: Nature Geoscience, v. 6, p. 380-384.

Triplehorn, D. M., 1965, Origin and Significance of Glauconite in the Geologic Sequence: Tulsa Geological Digest, v. 33, p. 282-283.

Trouw, R. A. J., Passchier, C. W., Simões, L. S. A., Andreis, R. R., and Valeriano, C. M., 1997, Mesozoic tectonic evolution of the South Orkney Microcontinent, Scotia arc, Antarctica: Geological Magazine, v. 134, issue 3, p. 383-401.

University of Minnesota, 2011, Tool for Microscopic Identification, https://tmi.laccore.umn.edu/tutorial/templates, accessed February 12, 2018.

Veizer, J. and Prokoph, A., 2015, Temperatures and oxygen isotopic composition of Phanerozoic oceans: Earth-Science Reviews, v. 146, p. 92-104.

Velde, B., 2005, “Green Clay Minerals,” Treatise on Geochemistry, Elsevier Ltd., v. 7, p. 309-324.

Villa, G., Fioroni, C., Persico, D., Roberts, A. P., and Florindo, F., 2013, Middle Eocene to Late Oligocene Antarctic glaciation/deglaciation and Southern Ocean productivity: Paleoceanography, v. 29, p. 223-237.

Zachos, J. C., Breza, J. R., and Wise, S. W., 1992, Early Oligocene ice-sheet expansion on Antarctica: Stable isotope and sedimentological evidence from Kerguelen Plateau, southern Indian Ocean: Geology, v. 20 issue 6, p. 569-573.

Zachos, J. C., Dickens, G. R., and Zeebe, R. E., 2008, An early Cenozoic perspective on greenhouse warming and carbon-cycle dynamics: Nature, v. 451, p. 279-283.

Zachos, J., Pagani, M., Sloan, L., Thomas, E., and Billups, K., 2001, Trends, Rhythms, and Aberrations in Global Climate 65 Ma to Present: Science, v. 292, p. 686-693.

Appendix

Table A-1: Major element index calculations

	Depth (mbsf)	Mn*	D Index	Si*	Age (mya)*
55R-06W 39-41cm	576.09	-0.769	0.604	12.7	34.30
56R-01W 5-7cm	577.95	-0.767	0.612	6.06	34.39
56R-01W 125-127cm	579.15	-0.975	0.445	8.72	34.45
56R-02W 88-90cm	580.28	-1.172	0.341	10.7	34.50
57R-01W 5-7cm	587.65	-0.895	0.358	8.22	34.86
57R-01W 105-107cm	588.65	-1.225	0.238	17.7	34.91
58R-01W 55-57cm	597.75	-0.560	0.720	7.21	35.35
58R-01W 87-89cm	598.07	-0.512	0.725	7.33	35.37
58R-02W 55-58cm	599.25	1.11	0.610	6.86	35.42

*****Ages calculated from sample depths and age model from Houben et al. (2013)

Table A-2: Particle size data of study samples from Light (2017)

Sample ID	Depth (mbsf)	Clay % (<2µm)	Silt % (<50 µm)	Sand % (<2000 µm)	Age (mya)*
56R-01W 5-7cm	577.95	37.24	38.36	15.58	34.39
56R-01W 125-127cm	579.15	14.19	62.64	10.82	34.45
56R-02W 88-90cm	580.28	7.98	30.30	50.17	34.50
57R-01W 5-7cm	587.65	11.77	65.88	11.98	34.86
57R-01W 105-107cm	588.65	9.52	37.56	41.23	34.91
58R-01W 55-57cm	597.75	11.25	60.68	16.15	35.35
58R-01W 87-89cm	598.07	6.20	39.75	34.46	35.37

*****Ages calculated from sample depths and age model from Houben et al. (2013)

Table A-3: Major element ICP-MS results in normalized weight percent oxide

	SiO_2	TiO_2	Al_2O_3	Fe_2O_3	MnO	MgO	CaO	Na_2O	K_2O	P_2O_5	Total
55R-06W 39-41cm	82.94	0.36	6.55	4.29	0.01	0.94	1.41	1.49	1.93	0.09	100
56R-01W 5-7cm	70.80	0.62	11.68	7.37	0.02	1.66	2.45	2.11	3.15	0.13	100
56R-01W 125-127cm	72.47	0.49	8.31	10.33	0.02	1.68	1.09	1.83	3.64	0.13	100
56R-02W 88-90cm	71.45	0.39	6.69	12.86	0.02	2.02	0.99	1.44	4.06	0.08	100
57R-01W 5-7cm	67.42	0.45	8.20	14.64	0.04	2.54	0.78	1.53	4.30	0.11	100
57R-01W 105-107cm	74.18	0.25	4.19	13.36	0.02	2.02	0.73	1.17	4.02	0.07	100
58R-01W 55-57cm	76.54	0.45	10.62	4.10	0.02	1.10	1.80	2.34	2.93	0.09	100
58R-01W 87-89cm	76.93	0.51	10.50	3.95	0.02	1.15	1.81	2.28	2.75	0.09	100
58R-02W 55-58cm	44.27	0.43	6.45	3.28	0.84	2.99	38.09	1.31	2.09	0.23	100

Table A-4: Trace element ICP-MS results in parts per million

	Sc	V	Cr	Co	Ni	Rb	Sr	Y	Zr	Nb	Cs	Ba	Hf	Ta	Pb	Th	U
55R-06W 39-41cm	8.48	70.00	53.05	4.55	18.49	75.30	126.31	18.03	157.88	7.11	3.02	419.47	4.32	0.49	2.15	7.61	3.87
56R-01W 5-7cm	12.64	89.99	67.85	7.18	25.58	115.76	182.28	22.47	190.10	10.80	4.63	559.21	5.13	0.79	2.57	13.01	3.75
56R-01W 125-127cm	14.34	92.12	94.86	4.83	19.45	128.67	154.86	18.28	240.06	6.51	4.01	404.50	6.01	0.55	2.36	9.29	2.25
56R-02W 88-90cm	11.59	100.65	129.81	3.86	15.50	189.39	112.64	13.10	186.32	7.92	7.15	313.10	4.71	0.46	6.94	5.19	1.59
57R-01W 5-7cm	12.65	106.92	93.62	6.56	22.61	188.77	100.30	18.00	195.61	7.40	6.62	290.68	5.01	0.55	4.70	7.83	2.25
57R-01W 105-107cm	10.34	86.19	108.57	4.21	12.05	193.68	74.20	12.40	110.39	3.50	5.87	198.42	2.59	0.32	5.56	4.10	1.20
58R-01W 55-57cm	10.24	70.79	50.80	5.27	13.47	94.63	245.37	19.04	220.67	5.81	2.53	626.96	5.43	0.55	6.93	5.88	1.56
58R-01W 87-89cm	11.24	80.74	54.91	5.68	15.70	101.31	247.06	21.70	250.54	7.59	2.82	644.33	6.03	0.78	3.38	7.60	1.96
58R-02W 55-58cm	4.10	41.23	28.45	3.19	9.40	44.70	384.25	10.71	120.41	4.63	1.31	292.73	3.00	0.31	1.99	3.48	2.33

Table A-5: Rare earth element ICP-MS results in normalized parts per million

	La	Ce	Pr	Nd	Sm	Gd	Tb	Dy	Ho	Er	Tm	Yb	Lu
55R-06W 39-41cm	50.33	42.72	34.39	26.97	16.45	11.16	9.26	7.99	7.07	6.58	7.01	7.14	7.42
56R-01W 5-7cm	77.46	61.19	47.30	38.21	23.97	14.46	11.83	10.32	8.89	8.32	8.49	8.80	8.58
56R-01W 125-127cm	64.04	54.50	40.36	32.02	19.75	12.55	10.11	8.30	7.32	6.67	6.94	6.91	6.73
56R-02W 88-90cm	40.54	36.49	28.77	22.53	13.63	9.24	7.77	6.21	5.35	4.79	5.14	5.14	5.10
57R-01W 5-7cm	54.54	48.76	36.69	28.92	17.66	11.65	9.65	8.16	6.97	6.44	6.71	6.63	6.45
57R-01W 105-107cm	29.61	29.17	23.15	17.53	11.09	8.39	7.26	5.97	5.07	4.19	4.47	4.30	3.88
58R-01W 55-57cm	58.75	53.76	40.02	33.12	21.27	13.58	10.73	9.02	7.88	7.12	6.91	7.52	7.29
58R-01W 87-89cm	66.28	58.97	43.36	35.38	22.15	14.17	11.58	10.00	9.01	8.15	8.30	8.58	8.39
58R-02W 55-58cm	3270	28.66	23.95	18.08	11.12	7.75	6.67	5.05	4.52	3.87	4.17	4.28	4.23

Figure A-1: X-Pert High Score Analysis of 56R-01W-125-127, Bulk Powder

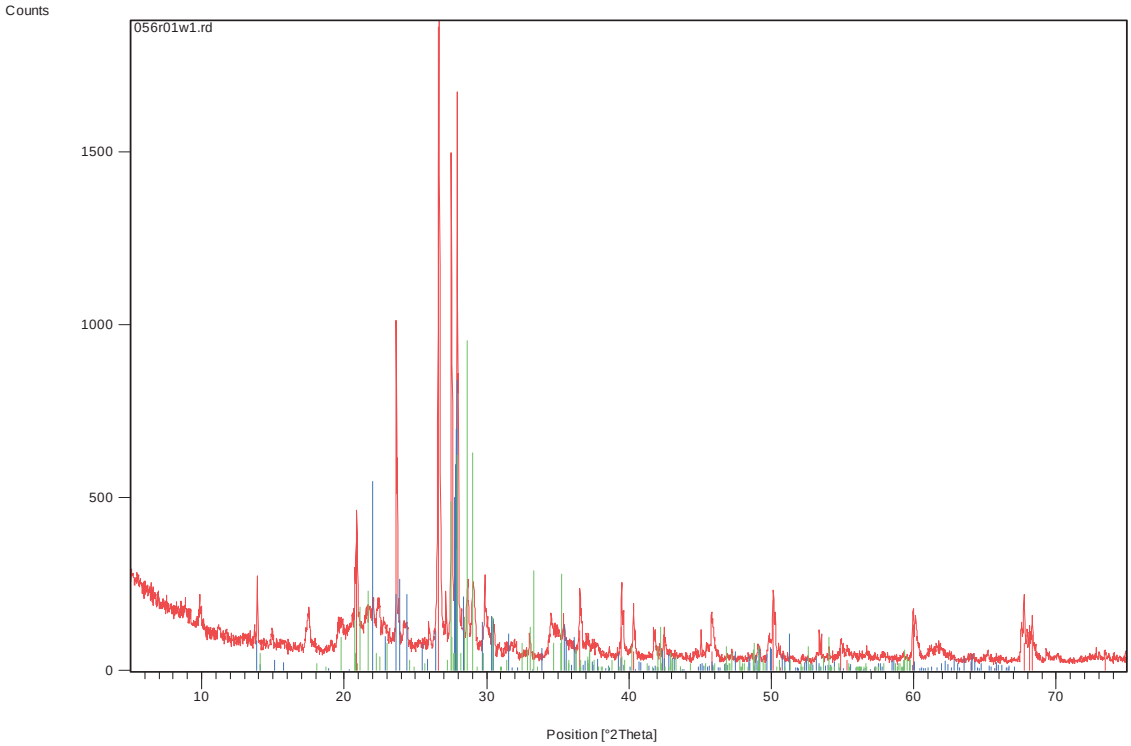

Pattern List:

Visible	Ref. Code	Score	Compound Name	Displacement [°2Th.]	Scale Factor	Chemical Formula
*	85-0930	50	Quartz	0.000	0.988	Si O2
*	76-0927	47	Albite calcian low	0.000	0.445	(Na0.84 Ca0.16) Al1.16 Si2.84 O8
*	50-0146	43	Potassium Magnesium Phosphate	0.000	0.507	K Mg P O4

Figure A-2: X-Pert High Score Analysis of 56R-02W-88-90, Bulk Powder

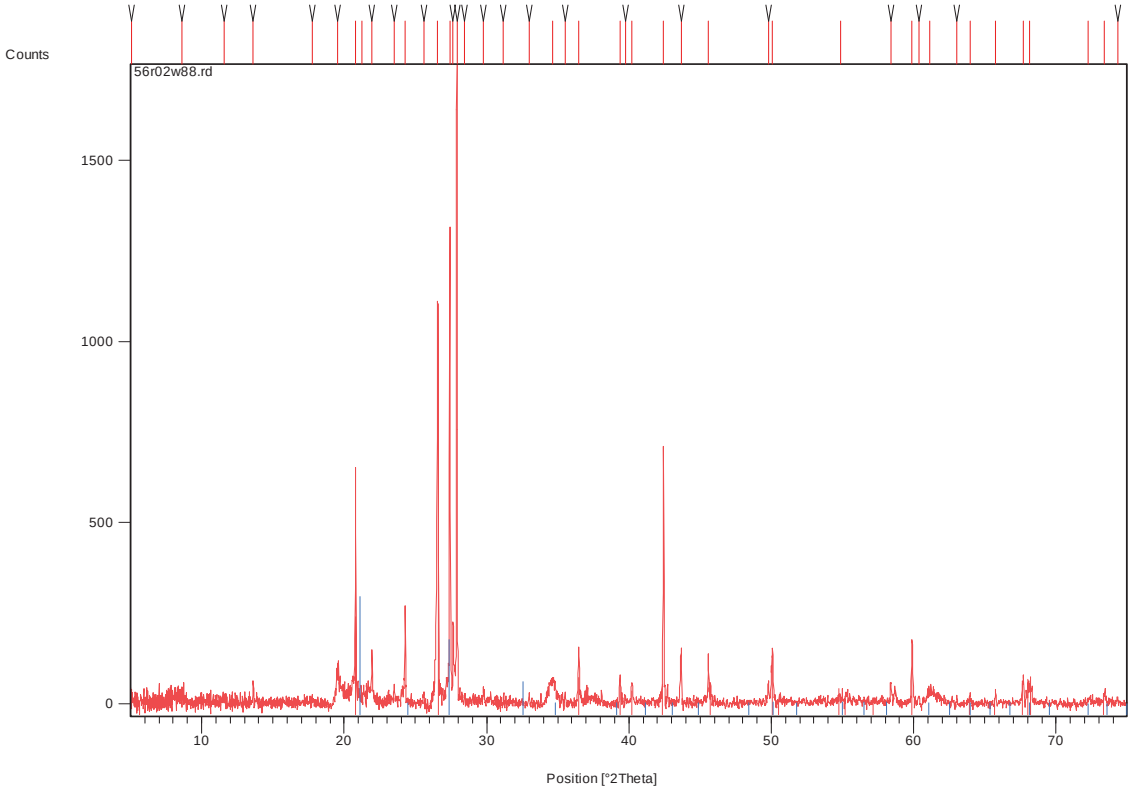

Pattern List:

Visible	Ref. Code	Score	Compound Name	Displacement [°2Th.]	Scale Factor	Chemical Formula
*	83-0539	68	Quartz	0.000	0.624	Si O2
*	86-1794	37	Eulytite, syn	0.000	0.167	Bi4 (Si O4)3

Figure A-3: X-Pert High Score Analysis of 57R-01W-5-7, Bulk Powder

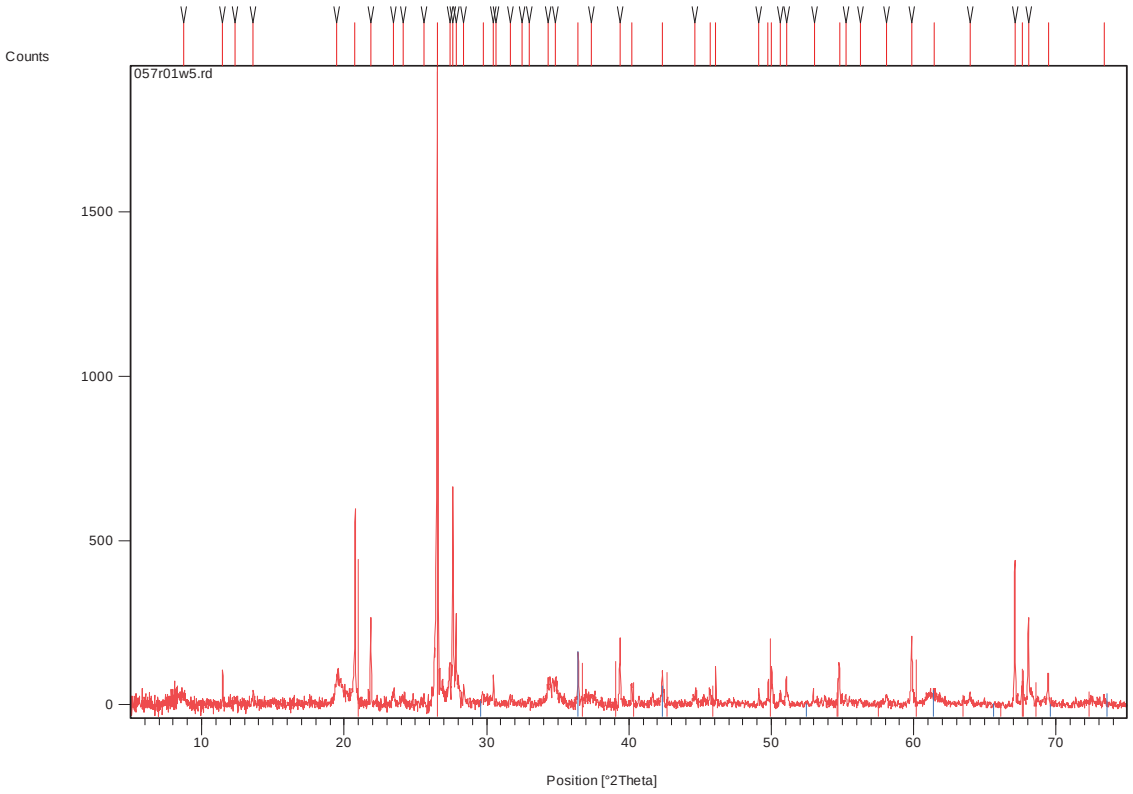

Pattern List:

Visible	Ref. Code	Score	Compound Name	Displacement [°2Th.]	Scale Factor	Chemical Formula
*	85-1780	35	Quartz	0.000	0.981	Si O2
*	78-2076	50	Cuprite	0.000	0.082	Cu2 O

Figure A-4: X-Pert High Score Analysis of 57R-01W-105-107, Bulk Powder

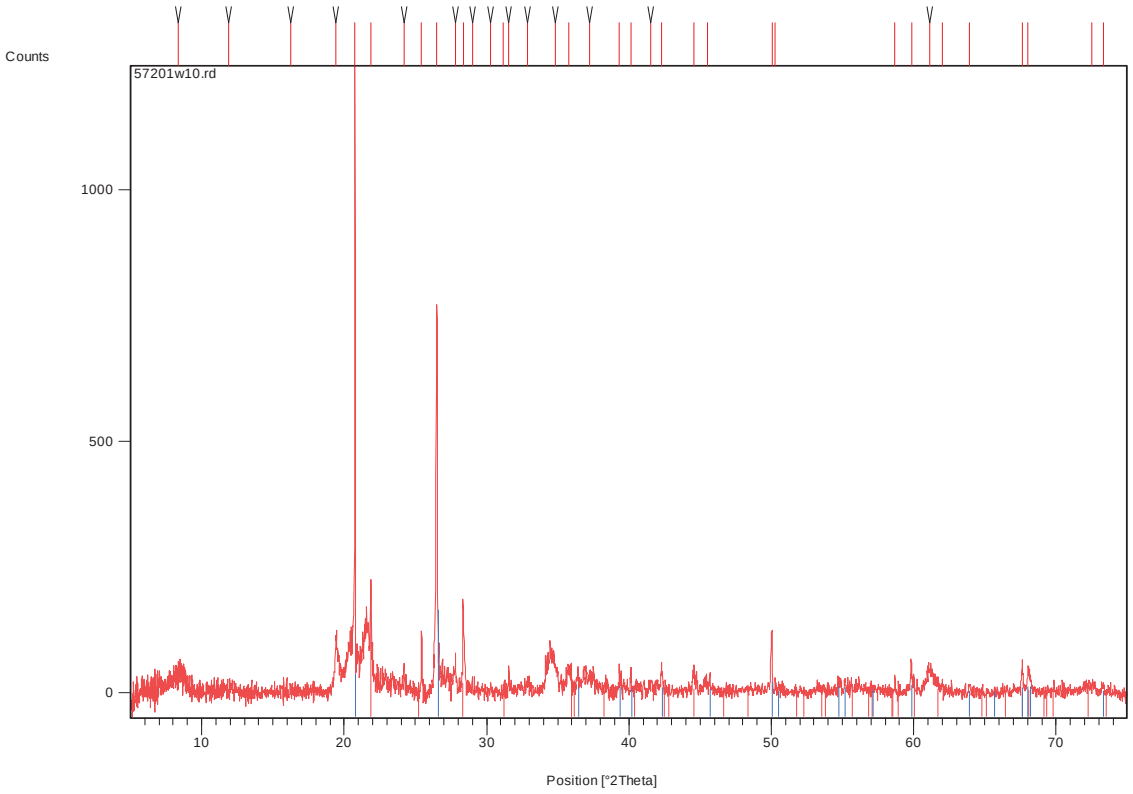

Pattern List:

Visible	Ref. Code	Score	Compound Name	Displacement [°2Th.]	Scale Factor	Chemical Formula
*	76-0938	52	Cristobalite low	0.000	0.177	Si O2
*	83-0539	50	Quartz	0.000	0.130	Si O2